JOURNAL OF GEOPHYSICAL RESEARCH, VOL. 97, NO. C6, PAGES 9669–9688, JUNE 15, 1992

Internal Hydraulics, Solitons and Associated Mixing in a Stratified Sound

JIANPING GAN AND R. GRANT INGRAM

Department of Atmospheric and Oceanic Sciences, McGill University, Montréal, Québec, Canada

Observations of tidally forced flow in a constricted and sill-like region of a highly stratified sound are examined as a problem of two-layer hydraulic exchange. Based on the current and salinity data, time and space dependent hydraulic conditions along the sound are discussed. It will be shown that the sound is subject to internal hydraulic controls at several locations, which account for the generation of strong internal hydraulic bores and drops in the upper layer. Internal solitary waves with 3-6 min period were found in the upstream propagating bore. Using results from different models of the solitary wave based on the Korteweg-de Vries (KdV) equation, it is shown that the second-order nonlinear term must be included in the two-layer model. Results from a first-order continuously stratified model, solved using the lowest mode eigenfunction, gave similar results as the second order two-layer model. This implies that two-layer models may ignore some properties of the real fluid and that internal solitons are also sensitive to the stratification characteristics of the water column. The vertical velocity shear, hydraulic characteristics of the flow and the presence of solitary waves were major contributors to vertical mixing in the sound.

INTRODUCTION

The interaction of a stratified flow with a sill and/or constriction is subject to internal hydraulic control. Internal bores or drops, which result from the effect of hydraulic control, can evolve into a packet of solitary waves due to nonlinear effects [*Maxworthy*, 1979]. This phenomenon has been observed in many areas, for example, in the Caspian Sea [*Ivanov and Konyaev*, 1976], Massachusetts Bay [*Halpern*, 1969; *Haury et al.*, 1979], Knight Inlet [*Farmer and Smith*, 1978], Observatory Inlet [*Farmer and Denton*, 1985], the Scotian Shelf [*Sandstrom and Elliott*, 1984], and on the Australian North West Shelf [*Holloway*, 1987].

In earlier studies on internal hydraulics, *Long* [1954] showed the results of various possible fluid configurations over an obstacle from an initially uniform flow upstream and downstream. *Baines* [1984] combined hydraulics with nonlinear wave theory in a study of the upstream bore and found that disturbances were governed by nonlinear effects and their character was determined by a balance between nonlinear steepening and dispersion of the wave. More recently, *Armi and Farmer* [1985], by using the conservation-energy equations and parameterizing flows in terms of the internal Froude number for each layer, examined the conjugate states for an internal hydraulic jump under the influence of two-way hydraulic control. The combined effect of a sill and a constriction was also discussed by *Farmer and Armi* [1986] and *Hogg* [1985].

Solitary waves, so called because they often occur as a single entity and are localized, include both nonlinear and dispersive effects. They are found at the front of a depression or an elevation apparently steepening due to nonlinear effects. With regard to modelling internal solitary waves, the *Benjamin* [1966] and *Ono* [1975] equation, the *Kubota et al.* [1978] equation, or the internal Korteweg-de Vries (KdV) [*Benny*, 1966] equation apply, according to whether the wavelength is much smaller, of the same order or much larger than the total water depth, respectively. However, *Maxworthy* [1979] concluded that the KdV equation could be used to crudely model events for a deep ocean. *Segur and Hammack* [1982] and *Koop and Butler* [1981], based on their two-layer experimental data, found that the KdV predicted the solitary waves with remarkable accuracy, much better than finite-depth theory. Until now, most oceanographers used the KdV to explain observational data. For example, *Osborne and Burch* [1980] and *Pierini* [1989] applied the KdV equation to understand internal wave fields in the Andaman sea and the Alboran Sea, even though their observed wavelengths were comparable to the total water depth. Despite the relative depth limitation, the KdV equation can include shear [*Liu and Benny* 1981; *Tung et al.*, 1981; *Maslowe and Redekopp*, 1980], topography, variable cross-section [*Johnson*, 1973*a,b*; *Grimshaw*, 1977], viscous effects and higher-order effects [*Koop and Butler*, 1981]. Based on our observations, we will focus on the KdV equation.

The importance of hydraulic jumps on mixing in estuaries has been discussed by several authors, e.g., *Partch and Smith* [1978], *Gardner and Smith* [1978], *Lewis* [1985]. They indicated that intense mixing events were either initiated or coincided with the existence of critical or supercritical flow. *Sandstrom and Elliott* [1984] found that the dissipation of solitary waves associated with a shoreward propagating internal tide could provide energy for vertical mixing.

The object of this paper is to gain insight into the characteristics of hydraulics, solitons and their effects on the mixing along a well stratified sound. Based on current and salinity data, it will be shown that hydraulic critical conditions lead to the generation of strong bores and drops. The internal "bore" and "drop" in this paper are defined as a sudden upward and downward steepening of the density interface, respectively. Spatial and temporal characteristics of the high-frequency internal waves are considered on the basis of hydraulic results and KdV theory. After discussing the mechanisms of internal hydraulics and high-frequency waves, vertical mixing along the sound is considered.

STUDY AREA

Manitounuk Sound is a 60 km-long coastal embayment in southern Hudson Bay (Figure 1). Depth varies from 70 to 90 m near its entrance to less than 10 m near the inland termination. The average width in the sound is about 3 km with a horizontally constricted region of about 1.5 km near Paint Islands, and with a small island located about 5 km upstream of the constricted region. Two inlets inside the sound, Schooner and Boat Openings, connect it with Hudson Bay. The water exchange through both openings is minor and their effects are ignored [*Ingram et al.*, 1989]. In general, the sea ice cover is of the landfast type and forms in early December and breaks up in late June. The average ice thickness is about 1-1.5 m. At the entrance of the sound, the Great Whale River provides the

Paper number 92JC00491.
0148-0227/92/92JC-00491$05.00

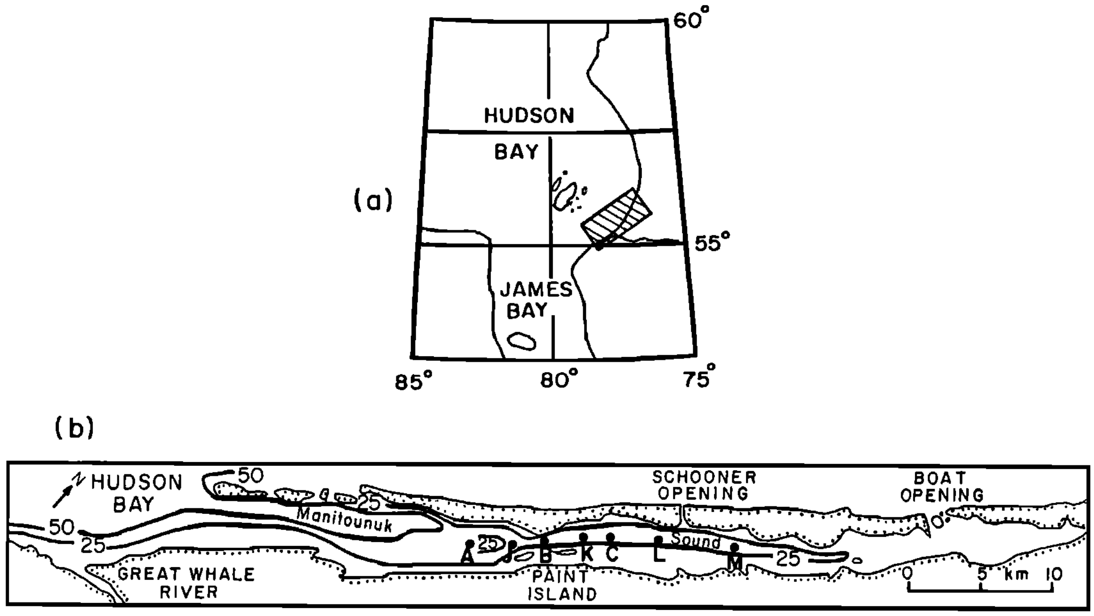

Fig. 1. Local bathymetry and station location in Manitounuk Sound.

only major freshwater source. Due to the intrusion of brackish water associated with the plume of the river and ice melt in spring, the sound can be characterized as highly stratified from mid-winter to early summer.

Previous studies have shown that the progressive thinning of the pycnocline and increasing salinity of the upper layer with distance into Manitounuk Sound are prominent features [*Ingram*, 1983]. Further details about conditions in the sound were described by *Ingram* [1981, 1983]. In particular, Ingram suggested that one of the sources of denser water for the upper layer was vertical exchange near Paint Island (Figure 1). A hydraulic mechanism which may increase vertical exchange was recently suggested by *Ingram et al.* [1989]. They assumed that the dissipation of high-frequency internal waves, generated at a constriction/sill, could cause upward salt transport across the pycnocline. However, their observations were taken every 5 min, resulting in an aliased description of the high-frequency (3-5 min period) fluctuations present.

OBSERVATIONS

Current meters (Aanderaa RCM 4 and RCM 7) were moored at stations A, B and C at depths of 1.5, 2.5 and 7.5 m below the underside of the ice, and sampled velocity, temperature and conductivity every minute from April 14 to May 2, 1989 (Figures 1 and 2). The distance between the individual stations was 5.2 km, with station A upstream of the small island, B at the narrowest section, and C downstream of the constriction. CTD (SBE 9) profiles were also taken at stations A, J, B, K, C, L, and M (Figures 2 and 3). Both accuracy and resolution of current meters and the CTD can be seen in Table 1. The predicted average tide amplitude was about 2 m during the observation period, with the peak value of 3.5 m occurring during the spring tide of April 23 (Figure 4).

CTD profiles showed relatively strong stratification in the sound, with the pycnocline at about 2.5-3.0 m beneath the ice cover. Below the pycnocline, the salinity increased smoothly with depth. Similar to a previous study by *Ingram* [1983], near-surface salinity gradually

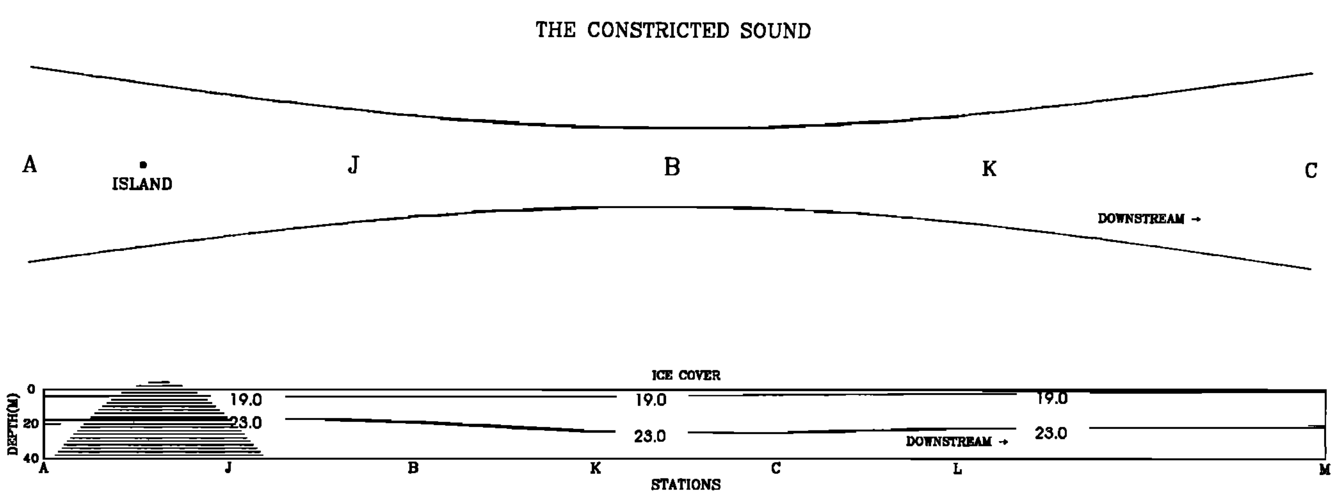

Fig. 2. Sketch showing plan view and σ_t transects in the sound.

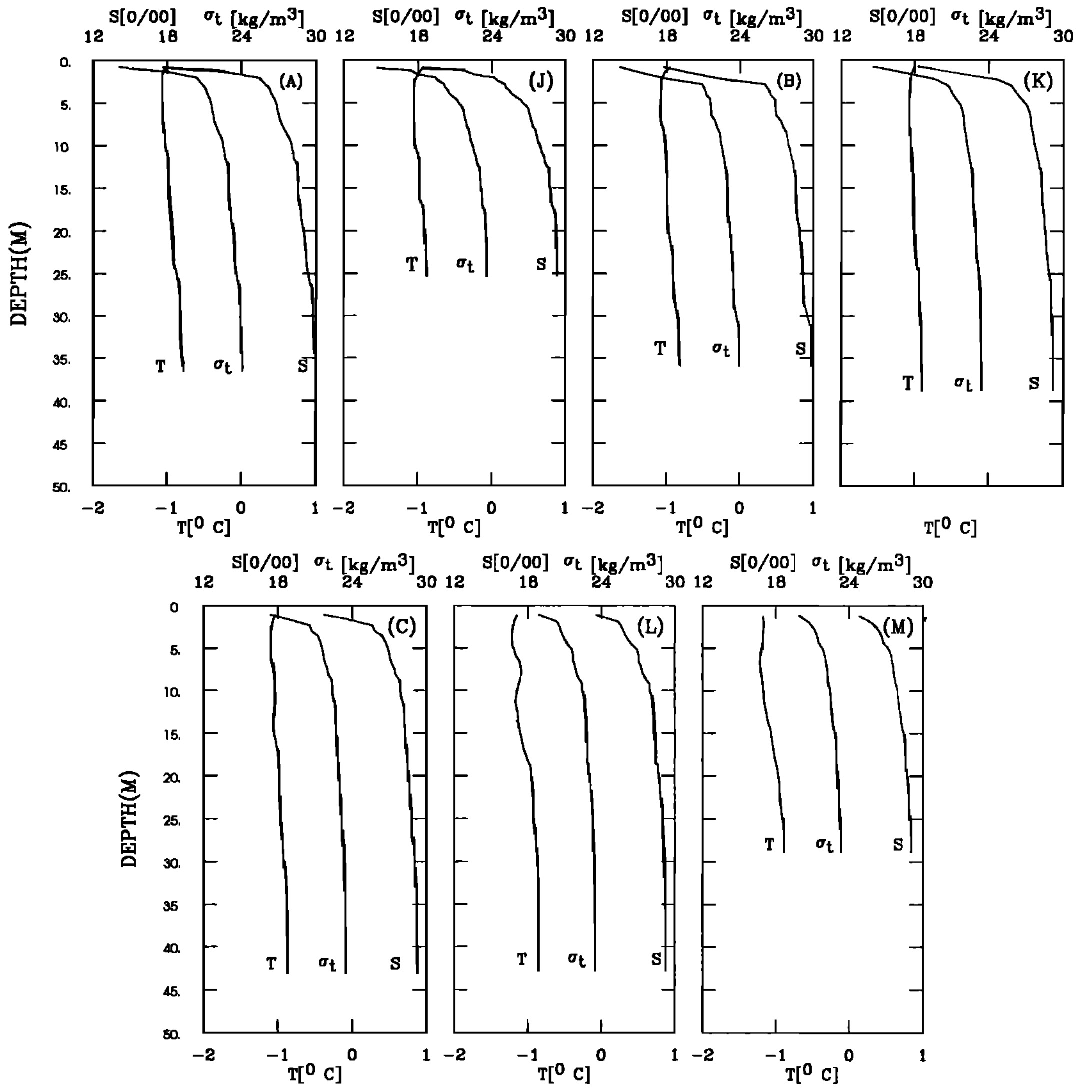

Fig. 3. Vertical profiles of salinity, temperature, and density (σ_t) for stations A, J, B, K, C, L, and M on April 29, 1989.

increased from stations A to M, with the largest increase from stations A to J and K to C (Figure 2). The smaller depth of station J was related to its location in a shallower region near the small island. The variations of temperature with depth were quite small at all stations. It should be noted that CTD observations were not made during spring tide, the focus of this study, because of unexpected problems. The average pycnocline depths during spring tide are estimated to be about 0.5 m deeper than at neap tide, similar to the observations of *Larouche* [1984].

Figures 5 to 7 present the time series of current, salinity, and temperature for spring tides. Because the cross-channel velocity components were much smaller than the along-sound velocity components, and the expected direction of propagation of the internal bores and high-frequency waves were also along the channel, the

TABLE 1. Accuracy and Resolution of Current Meters and CTD

	Accuracy	Resolution
	Aanderaa Current Meter	
Temperature	±0.05°C	0.01°C
Conductivity	±0.05 mmho/cm	0.05 mmho/cm
Direction	±5°	0.40
Speed	1 cm/s	0.2 cm/s
	SBE 9 CTD	
Temperature	±0.01°C/6 months	±0.001°C
Conductivity	±0.001 s/m/month	±0.001 s/m
Pressure	0.5% of full scale range	0.05% of full scale range

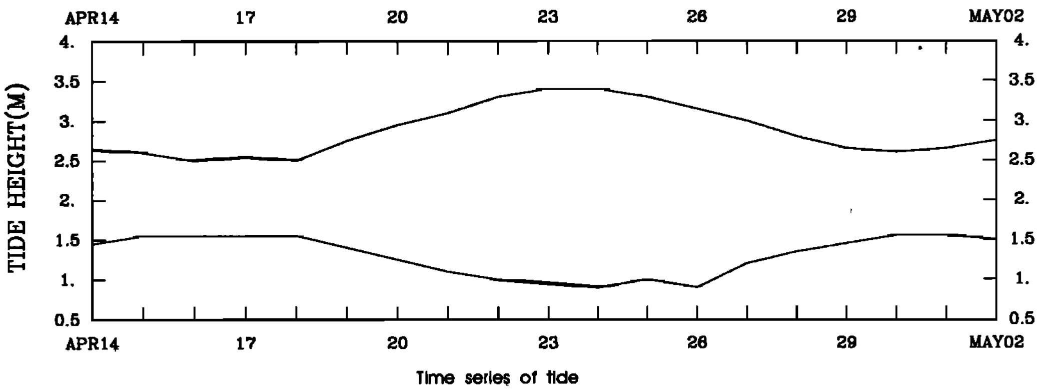

Fig. 4. Low tide (dashed line) and high tide (solid line) during the observation period based on predictions of the Canadian Hydrographic Service for 1989.

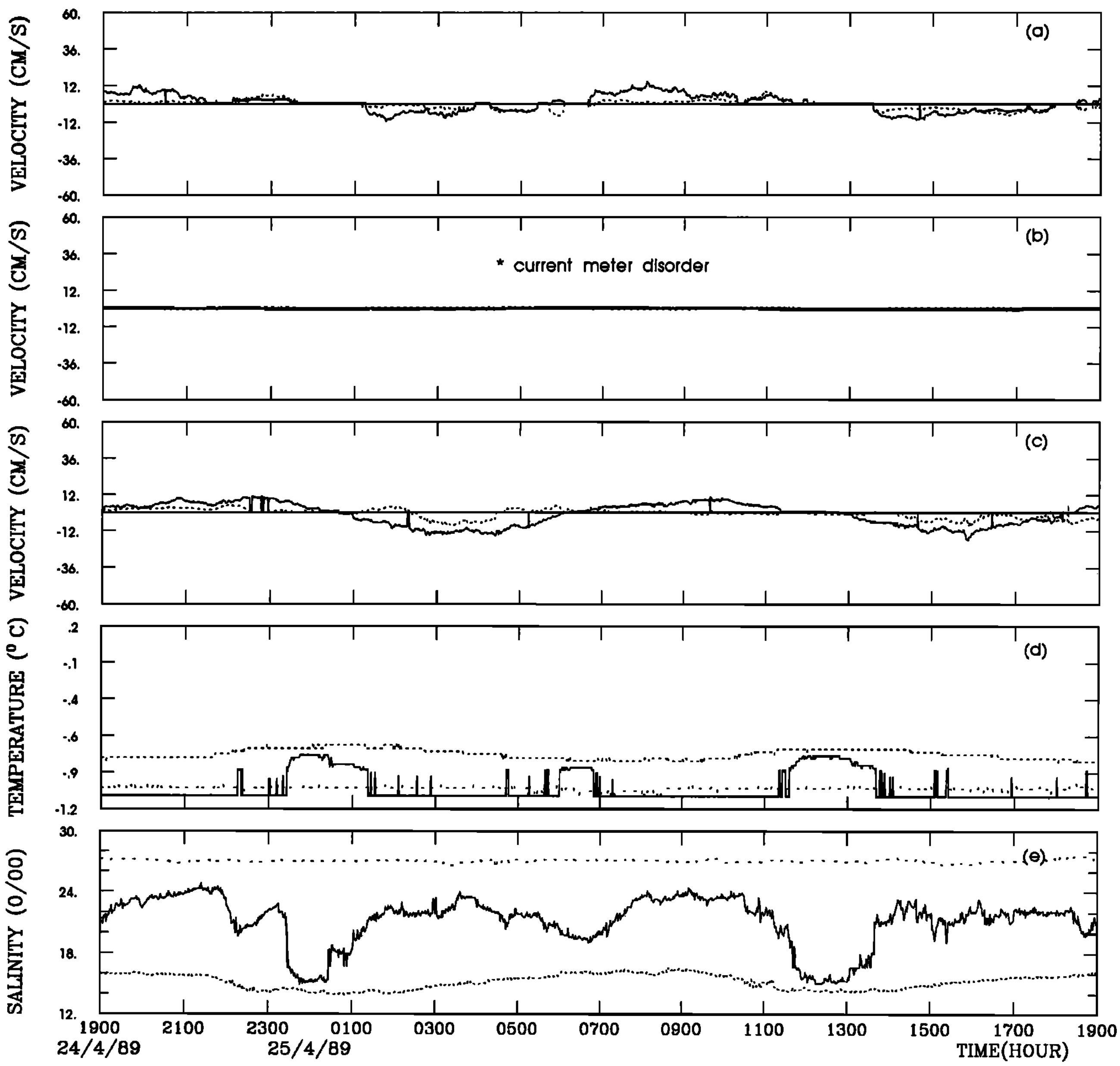

Fig. 5. Time series of current, temperature and salinity at station A during the spring tide: Velocities at (*a*) 1.5, (*b*) 2.5 and (*c*) 7.5 m (solid and dashed lines are for along- and cross-channel components, respectively), and (*d*) temperature and (*e*) salinity (Dashed, solid, and dotted lines are for 1.5, 2.5, and 7.5 m, respectively).

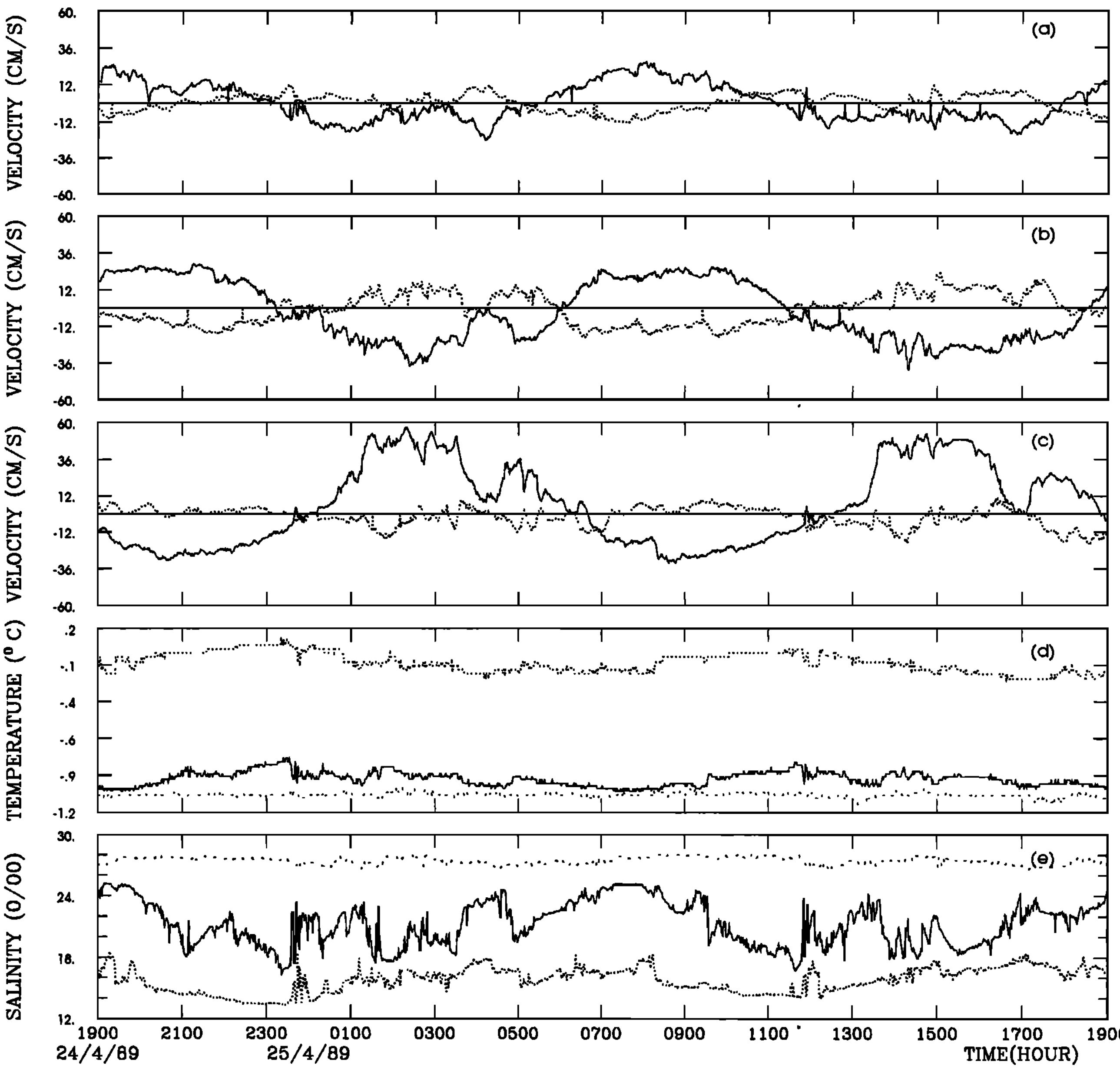

Fig. 6. Same as Figure 5, but for station B.

along-channel velocities will be the focus of our study. Here, positive velocities are directed into the sound (NE), corresponding to the flood, and negative velocities are directed out of the sound (SW), corresponding to the ebb. Tidal currents at 2.5 m (upper layer) and 7.5 m (lower layer) were generally opposed at station B. However, the whole water column at stations A and C moved in the same direction. The tidal flow was predominantly semidiurnal. The velocities at station A were much smaller than those at station B (at the constriction) and station C. More variance occurred in the velocity signal at the constriction than at stations A and C. During neap tide (not shown), the velocity was smaller and less variable at all stations.

Because of a malfunction in the 2. 5 m-deep current meter at station A, no velocity data were recorded. Data at 7.5 m for station C were edited to delete a few unrealistic pulses.

At our observation depths, temperature was in general negatively correlated with salinity. The temperature slowly decreased with depth. The average temperature and Δ_t are listed in Table 2.

Examining the along-channel salinity field, we found that the salinity difference between downstream and upstream stations (ΔS) (Figure 8) was generally positive; however, a slight decrease occurred at 2.5 m between stations A and B during spring tides. At the time scale of the semidiurnal tide, fluctuations in salinity were prominent at the upper two observation depths (Figures 5e, 6e and 7e). At station A, strong drops in S were observed at 2.5 m when the tide changed from flood to ebb for both the neap and spring tide. At station B, from peak flood to the beginning of ebb, salinity dropped steadily at 2.5 m in the initial stages, then increased sharply by about 6‰ in a few minutes. Strong salinity bores were superimposed on the tidal signal. High-frequency variations of salinity were also evident in some of the strong bores at spring tides, on the shift from flood to ebb. Similar, but weaker, signals were also observed at 1.5 m. During spring tides at station C, a salinity bore at 1.5 m, followed by a drop at 2.5 m, occurred during the flood (Figure 7). A fluctuation also appeared in the temperature field but not in

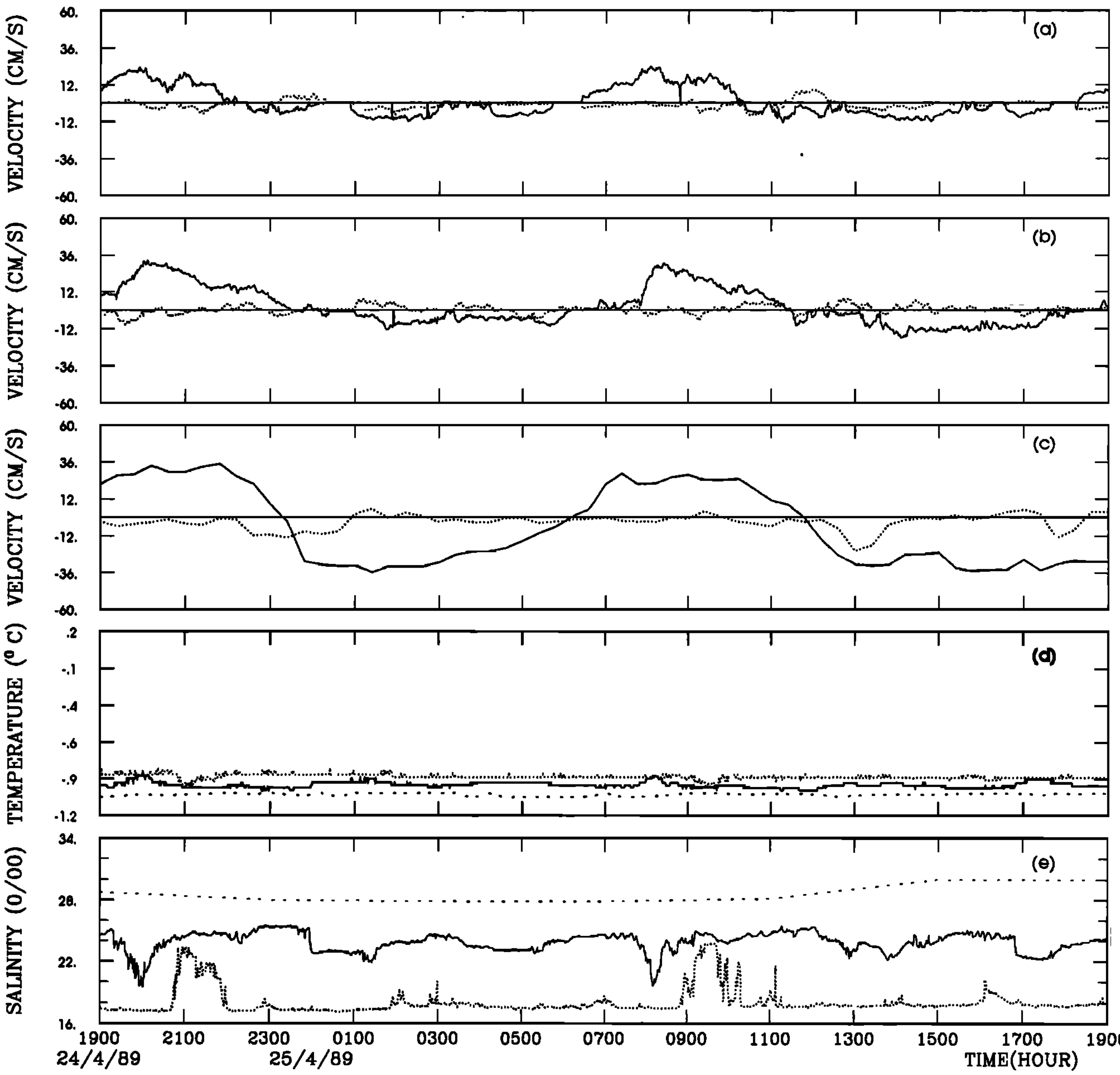

Fig. 7. Same as Figure 5, but for station C.

velocity at 1.5 and 2.5 m. Assuming linear salinity gradients between measured levels and conservation of salinity, the computed isohaline contours from 1.5 to 7.5 m are shown in Figure 9. The maximal drop at station A of 3-3.5 m amplitude occurred at a depth of about 3 m during the spring tide and a depth of 2.5 m during the neap tide (not shown). At station B, the high-frequency wave signals extended from the surface to a depth of 5.5 m during spring tide. The maximum high-frequency wave depression dropped from a depth of 2.5 m to

TABLE 2. The Average Temperature and σ_t for Three Stations at Current Meter Depths

		Instrument Depth, m					
		Neap Tide			Spring Tide		
	Station	1.5	2.5	7.5	1.5	2.5	7.5
Temperature, °C	A	-0.7	-1.0	-1.1	-0.8	-1.0	-1.0
	B	0.1	-0.9	-1.1	-0.1	-0.9	-1.1
	C	-0.8	-0.9	-1.1	-0.9	-1.0	-1.0
σ_t, (kg/m^3)	A	9.3	15.8	21.7	12.0	17.0	22.1
	B	10.9	16.0	21.9	12.6	17.1	22.1
	C	13.1	17.6	21.8	14.5	19.1	22.9

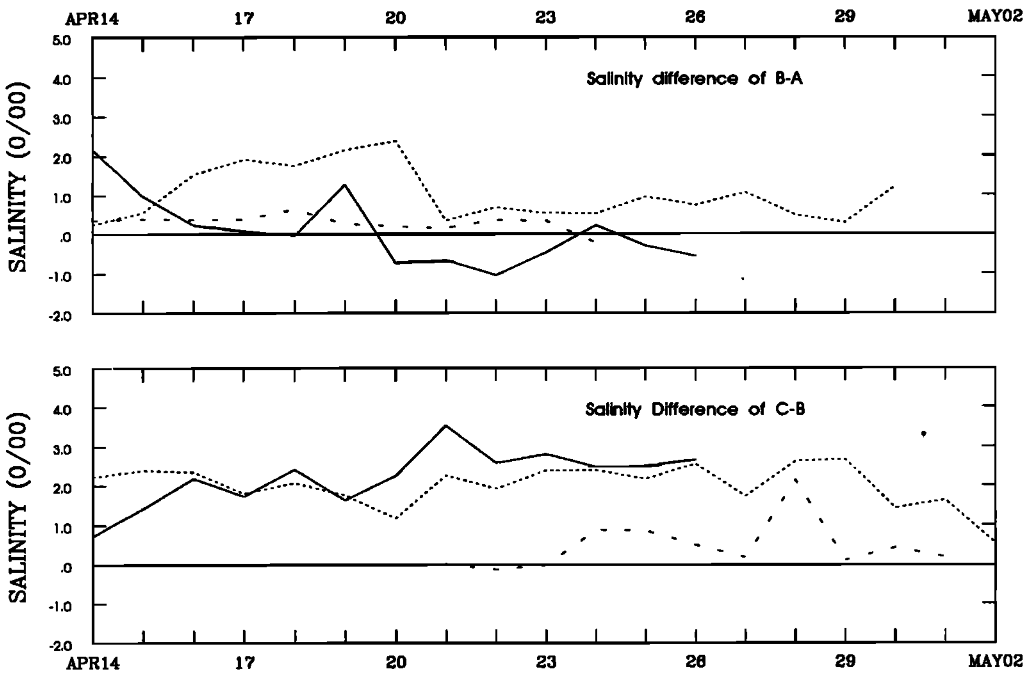

Fig. 8. Time series of salinity difference between (*a*) station B and A, and (*b*) station C and B. Dashed, solid, and dotted lines refer to depths of 1.5, 2.5, and 7.5 m, respectively.

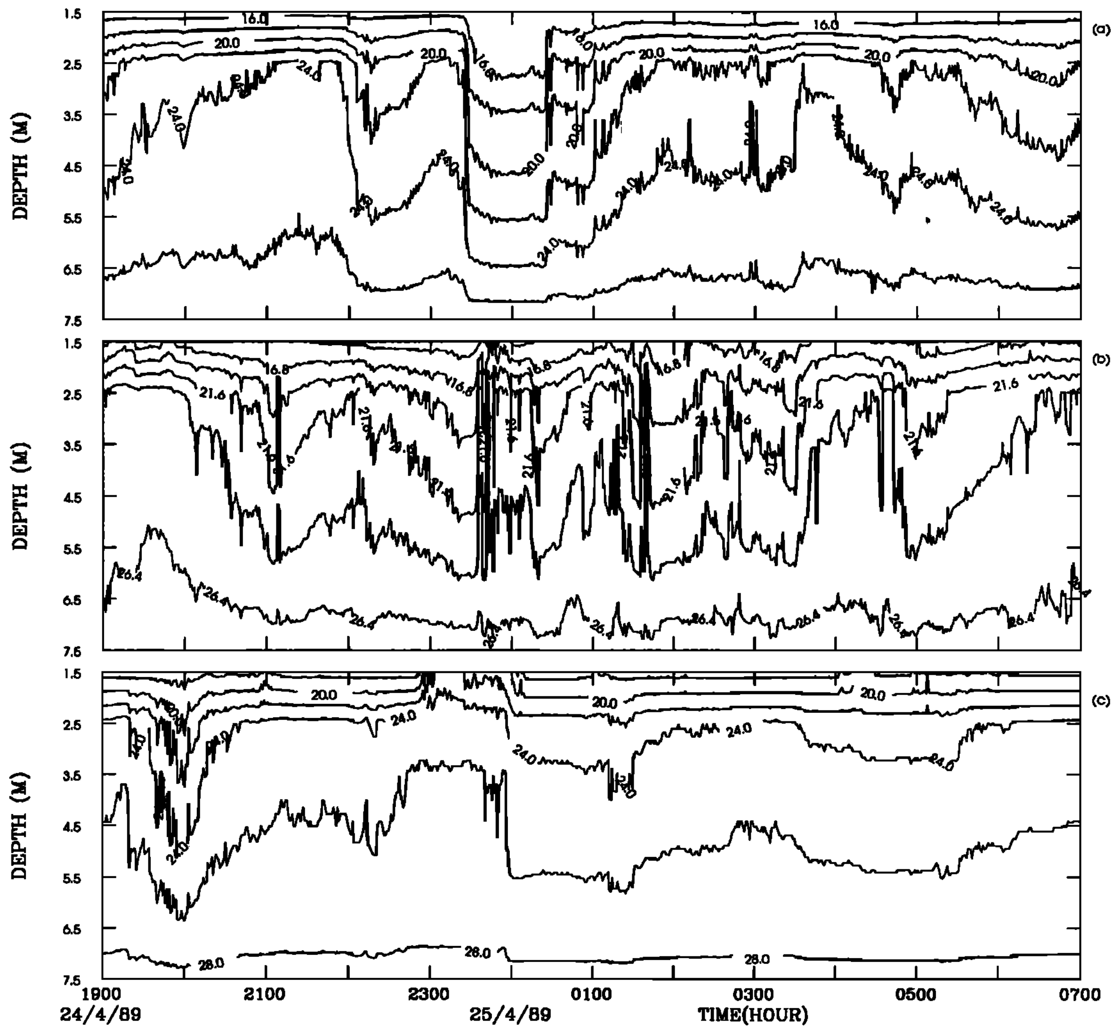

Fig. 9. The computed isohaline contours based on an interpolation of observations at discrete depths at stations (*a*) A, (*b*) B and (*c*) C during spring tide.

4.5 m. The drop at station C, shown in Figure 9c, spanned from 2.0 to 6.5 m depth. The vertical salinity gradients were reduced when hydraulic drops, bores and solitary waves occurred.

Similar to the high-frequency internal oscillations in salinity at station B, temperature and velocity fluctuations were also observed when the upper layer flood decreased and swung to ebb. However, the presence of a very small vertical gradient of temperature and velocities between 2.5 and 7.5 m during the period of high-frequency fluctuations does not allow easy identification of the high-frequency signal in both temperature and velocity records. The high-frequency fluctuations appeared very much like the decomposition of a bore perturbation into a sequence of high-frequency depression waves. The periods of the waves were estimated at about 2-6 min, some longer than the values of 2-3 min suggested by *Ingram et al*.[1989]. The oscillations were in a packet of approximately three to six with the strongest arriving first. The oscillations are considered to be solitary waves. Their amplitude can also be estimated from the equation

$$\text{AMPLITUDE}_{\text{soliton}} = \frac{\Delta S}{\partial S/\partial Z} \tag{1}$$

where ΔS is the salinity increase due to crest steepening of the wave and $\partial S/\partial Z$ is the salinity gradient. In our case, the amplitude (crest-trough) was estimated at about 2-3 m. Because of abnormally lower winter run-off of the Great Whale River during the observation period(100 m^3/s) in 1989 compared to other years, the stratification was weaker than normal. Hence, both hydraulic bore/drop and solitary waves may differ during years of stronger river discharge.

Individual bore and solitary wave events were not followed between stations. Thus, the data could not provide a measure of the phase speed nor the direction in which the wave propagated. In fact, it could be only deduced from the data at station B that the propagation was mainly in the upstream direction, i.e., towards the entrance of the sound.

INTERNAL HYDRAULICS

An earlier study of hydraulic theory [*Long*, 1953] showed that one important parameter which characterizes hydraulic control is the Froude number:

$$F = \frac{u}{(gH)^{\frac{1}{2}}} \tag{2}$$

where u and H are the flow speed and total water depth. It is obvious that the long waves cannot propagate upstream against flow when F=1 or $u=(gH)^{1/2}$, and information about downstream conditions cannot pass the control where F=1. Hence, the place where F=1 controls the flow. For two-layer flow, the necessary condition for an asymmetrical interface under steady conditions is that the flow be subject to the control condition, G^2=1 [*Armi and Farmer*, 1986]. G is the composite Froude number:

$$G^2 = F_1^2 + F_2^2 \tag{3}$$

where $F_i^2 = u_i^2/g'h_i$, i=1, 2 refers to upper and lower layer, and g' is reduced gravity. The Bernoulli equations for two layers in a constricted sound are

$$\frac{u_1^2}{2g} + h_1 + h_2 + \frac{P}{\rho_1 g} = \text{const}_1 \tag{4}$$

$$\frac{u_2^2}{2g} + \frac{\rho_1}{\rho_2}h_1 + h_2 + \frac{P}{\rho_2 g} = \text{const}_2 \tag{5}$$

with continuity equations,

$$Q_1 = u_1 h_1 b = \text{const}_3 \tag{6}$$

$$Q_2 = u_2 h_2 b = \text{const}_4 \tag{7}$$

which are combined to give

$$\frac{Q_1^2}{2h_1^2 b^2 g} + h_1 + h_2 + \frac{P}{\rho_1 g} = \text{const}_1 \tag{8}$$

$$\frac{Q_2^2}{2h_2^2 b^2 g} + \frac{\rho_1}{\rho_2} h_1 + h_2 + \frac{P}{\rho_2 g} = \text{const}_2 \tag{9}$$

where b, Q_i and ρ are the width, discharge and density in the sound. P is the pressure at the surface and const$_i$ (i =1,2,3,4) are constants. Differentiating equations (8) and (9) with respect to the flow direction x, and combining them together, we have

$$\frac{-u_1^2}{gh_1}\frac{dh_1}{dx} + \frac{u_2^2}{gh_2}\frac{dh_2}{dx} + \frac{1}{b}\frac{db}{dx}\left(\frac{u_2^2}{g} - \frac{u_1^2}{g}\right) + \frac{\rho_2 - \rho_1}{\rho_2}\frac{dh_1}{dx} = 0 \tag{10}$$

If $h_1+h_2=H$=const, (10) becomes

$$(1-G^2)\frac{dh_1}{dx} = \frac{1}{g'b}\frac{db}{dx}(u_1^2 - u_2^2) \tag{11}$$

It is apparent that the flow can be critical (G^2=1) when db/dx=0 (i.e., at the constriction). The control when $u_1=u_2$ is called a "virtual" control, which does not occur at a minimum area section [*Armi*, 1986]. Similarly, the control condition for flow over a sill is

$$\frac{dh_1}{dx}(1-G^2) = F_2^2\frac{dh}{dx} \tag{12}$$

and the critical flow occurs when dh/dx=0 (i.e., at the sill crest). The parameter, h, is sill height and $H=h_1+h_2+h$=const. For the combination of a sill and constriction, equations (11) plus (12) should be considered at the same time. The composite condition is given as

$$(1-G^2)\frac{dh_1}{dx} = \frac{1}{g'b}\frac{db}{dx}(u_1^2 - u_2^2) + F_2^2\frac{dh}{dx} \tag{13}$$

Obviously, the control here is a virtual control. More details are given by *Armi* [1986]. If the flow is subcritical upstream ($G^2 < 1$) and critical at the sill or narrowest section, it will be supercritical ($G^2 > 1$) downstream of the sill or narrowest section. Supercritical flow downstream can be matched to the subsequent subcritical flow by the presence of an internal hydraulic bore or jump. As shown in the data, Manitounuk Sound stratification can be approximated by a two-layer representation. To calculate Froude numbers during a tidal cycle, the positions of the interface are estimated by tracing the S=24 ‰ contours (cubic spline fitted). The current speed is taken from nearby current meters above or below the interface. Figure 10 shows the internal Froude number at stations B and C throughout the tidal cycle, corresponding to the time series in Figures 6 and 7. Froude numbers at station A were close to zero over the tidal cycles. Values of Froude numbers were averaged over 12 min intervals to delete high-frequency fluctuations. For the three stations, F_2^2 was approximately equal to zero because of the deep lower layer. Consequently, composite Froude numbers G^2 were dominated by the upper layer Froude number (i.e., $G^2 \approx F_1^2$). The time dependence of G^2 implies that the hydraulic control along the sound varied during a tidal cycle. Two events approaching critical (G^2=1) or even supercritical flow occurred at station B during maximum flood (inflow of

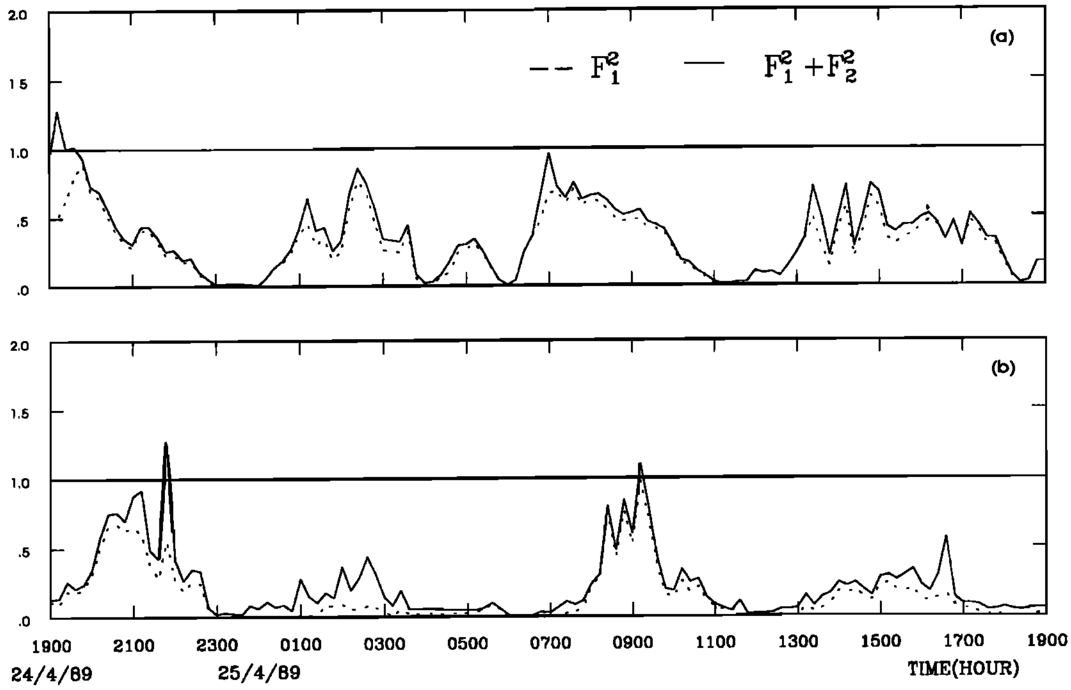

Fig. 10. Time series of composite Froude number at (*a*) station B and (*b*) station C on April 24 and 25, 1989. The composite Froude number at station A was close to zero.

upper layer). Supercritical flow also occurred at station C, just after maximum flood, and may indicate a control downstream of the narrowest section, as will be discussed subsequently.

Based on the time series of Froude numbers along the sound as shown in Figure 10 and two-layer hydraulic theory, the corresponding side and plane view of the two-layer hydraulic control flow through the constriction and small island are shown in Figure 11 for spring tide. Three possible interface configurations at different stages of the tide are explained as follows. Our aim is to explain the periodic bores (or drops) and interface tilt along the sound (Figures 5, 6, and 7 or 9).

Case 1 shows conditions two hours before maximal flood. The critical condition occurred at the narrowest region with subcritical conditions at both stations A and C. Just downstream of station B, supercritical conditions were highly likely because of the effects of constriction control [*Gan*, 1991]. As the flow approached $F_1^2 > 1$, the interface rose. After the flow passed the region of $F_1^2 < 1$, the bore was generated. The corresponding bore can be found at station B (Figure 6), which resulted from upstream propagation as the flood tide weakened and turned to ebb. The bore might not occur at the constriction during the ebb because bores were not observed at station B during the following flood.

Case 2 corresponds to the condition at maximal flood. Supercritical conditions occurred at station C. Since the flow upstream was subcritical, there must be a continuous transition from subcritical to supercritical flow downstream. The one hour lag between the time of critical flow at station B and supercritical conditions at C suggests a critical condition might occur between stations B and C (Figure 1 and 11) instead of at B. This resulted from the control at the narrowest section which could have caused the upper layer downstream to approach critical conditions by shallowing the upper layer asymptotically. A corresponding bore was generated near station C (Figure 7). The shallower interface near station C resulted in a bore at the 1.5 m level instead of at the lower level. At the downstream side of the small island near station A, the slope of the sill-like feature greatly reduces the total water depth to less than 10 m near the island. During the flood, the shallow area near the island might have increased F_2^2 dramatically, and hence generated critical and supercritical flow. When the flow matched subcritical flow downstream, the drop was generated. Relaxation of flooding allowed the drop to move back upstream. The flattening of the drop trough at station A (Figure 5) implied that the pycnocline was close to the bottom. A drop was also generated during the ebb, west of the island (case 3). However, a much weaker drop signal in station A implied that this ebb-drop (generated during ebb) did not pass, but only came close to station A. The drops shown at 2.5 m depth at both stations B and C (Figures 6 and 7) can be thought of as downstream propagation of an ebb-drop (during ebb) from station A when the tide slackened and turned to flood. Time series observations of the internal drop as it travelled downstream showed that it always arrived at about the same tidal phase for both station B and C. If we approximate the bore propagation speed by the phase speed of a nonlinear wave (see next section), the time when the drop appeared at station B was equal to the arrival time of the drop propagating from station A. However, the propagation towards station C from B might take a longer time, since the subsequent ebb would reduce the travel speed of the drop. Since drops were generated upstream where the interface was deeper, they were more apparent at 2.5 m, closer to the interface there.

At the beginning of the ebb (between cases 2 and 3), there were no controls along the sound. The bores generated downstream during cases 1 and 2 were passing through station B by this time. Some of the bores were modified to form a high-frequency internal wave train propagating continuously upstream, as will be discussed in the next section.

It should be noted that the bore was generated when the upper layer flow moved towards the supercritical region (i.e., decreasing upper layer depth h_1), and the drop occurred when the lower layer moved towards the supercritical region (i.e., decreasing lower layer depth h_2).

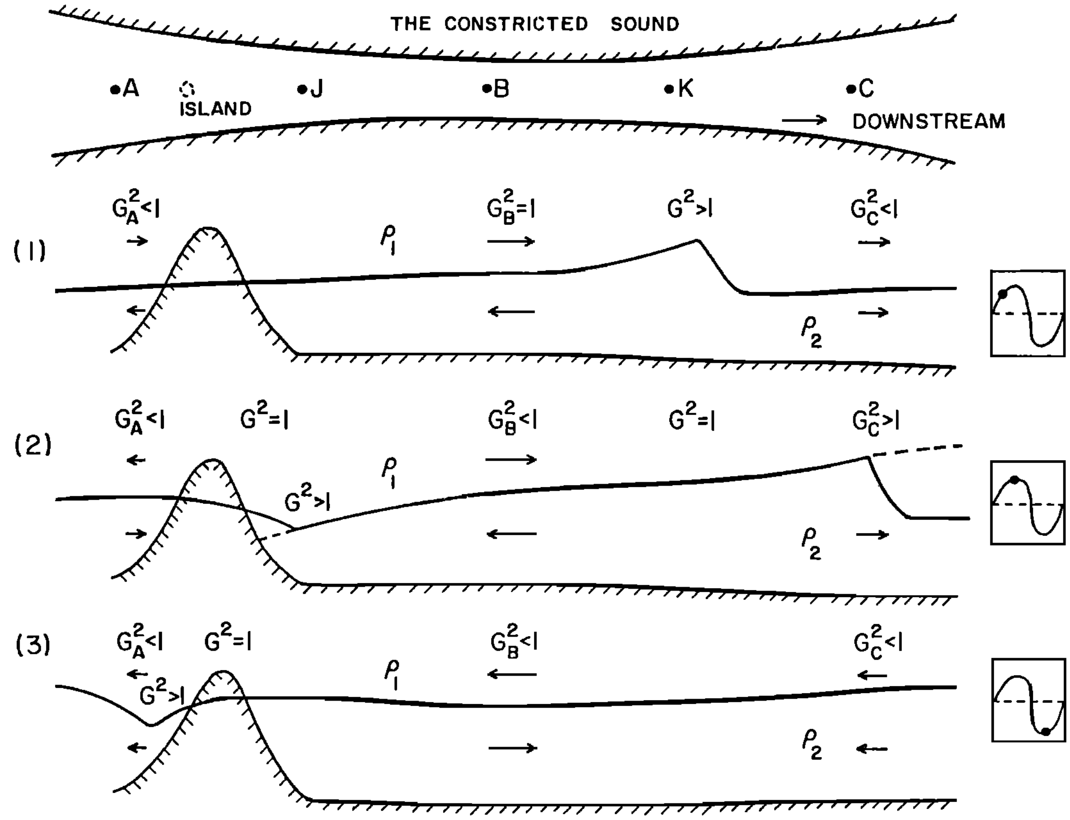

Fig. 11. Plane and side view of four possible interface configurations in the Manitounuk Sound during spring tide, for different stages of spring tide.

Conditions for the two supercritical flows (case 2) are similar to those for maximum exchange flow [*Armi and Farmer*, 1987], since disturbances at the interface cannot propagate through the region between these two supercritical flows from outside or inside. The exchange rate between the two bounding supercritical flows is maximal under such circumstances. Therefore, hydraulic processes depend only on the conditions between the two bounding supercritical areas. However, both cases 1 and 3 give submaximal exchange, and will always be influenced by one of the reservoir conditions [*Armi and Farmer*, 1985].

The continuity and energy equations (equations (7) and (10) of *Armi and Farmer* [1986]) in which the flow is parameterized in terms of the internal Froude number for each layer, are used to diagnose the possible critical states near the narrowest section. The possible pairs of F_1^2 and F_2^2 from both continuity and energy equations during a tidal cycle are averaged to get the general result (Figure 12). Figure 12 shows that the flow-rate line intersects the critical line, $G^2=F_1^2+F_2^2=1$, at $F_1^2\approx 1$ and $F_2^2 \ll 1$, which is consistent with the analytical results above. There are two solutions for the energy equation, with one of them coinciding with the continuity equation solution. The other solution predicts no control but supercritical internal Froude-number pairs, which is obviously not the case in the sound.

The theoretical results, both for bore generation and interface tilt, are in good agreement with observations. It is important to keep in mind that the control condition was dominated by the upper layer flow due to the deep lower layer except near the island. However, it should also be noted that the small island near station A may have more effect on the hydraulic characteristics in the sound than those discussed above. For further understanding, more observations near the small island are required. There are also a number of complications that have not been included in our discussions, for example, additional geometrical factors, frictional effects, under-ice keels and possible convergence or divergence of the flow.

GENERATION OF INTERNAL SOLITARY WAVES IN THE SOUND

Figure 6 and the expanded time series plots (Figure 13) demonstrate clearly the presence of high-frequency internal solitary-like waves in a disintegrating bore at station B, 30 min after the tide turned from flood to ebb. Significant density changes took place within a relatively small time interval. Fluctuations of both salinity and temperature were quite large for the leading wave. The maximal peak-trough amplitudes and wave period are listed in Table 3. In a continuously stratified fluid, water movements are not limited to this range of amplitude but extend through the water column above and below the pycnocline. As seen in Figure 13a, the water parcels dropped sharply to about 6 m depth, which caused the isohaline compression in front of the solitary wave.

The generation mechanism of these solitary waves was ascribed to the upstream propagation of a bore at the start of the ebb. This bore, characterized as a stepwise variation of the isohaline level, was generated during the flood tide downstream of the hydraulic control (discussed in section 3). During the upstream propagation of the bore, a packet of solitary waves evolved from the bore due to nonlinear effects. In particular, the nonlinearities increased rapidly at the narrowest section, as found by *Grimshaw* [1978] for his variable-coefficient KdV model and *Farmer*'s [1978] observations in Babine Lake. Our data show that the transition of the bore appeared very much like the decomposition of a stepwise perturbation into a sequence of solitons, which is quite similar to the

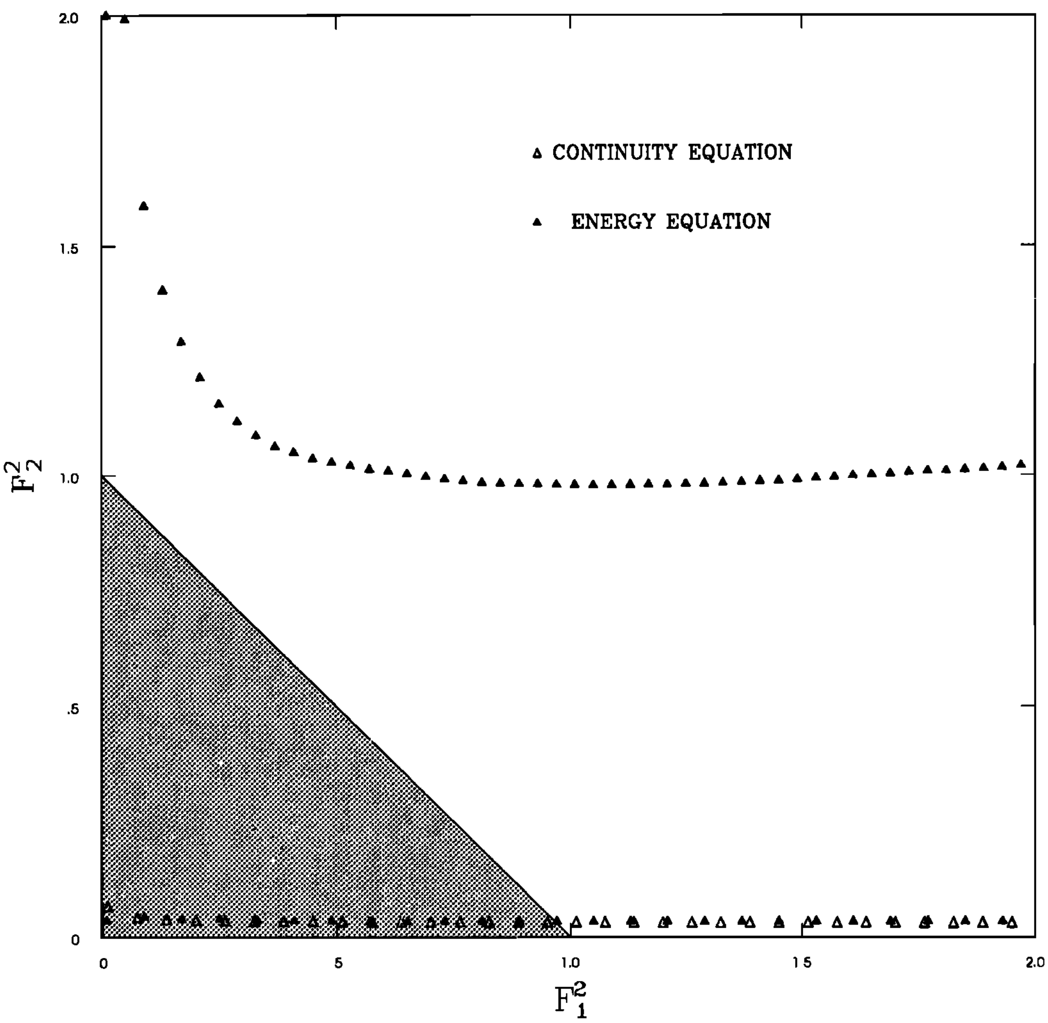

Fig. 12. Froude number plane showing solution to continuity and energy equations.

observation of a bore in the Caspian Sea by *Ivanov and Konyaev* [1976], and the laboratory results of *Baines* [1984]. The numerical simulation of the decomposition of a smoothed "step" into solitons has also been studied by *Lee and Beardsley* [1974]. The waves in the sound occurred as a depression of the streamline, as expected for the stratification in the sound.

From station B data, the soliton was decomposed from a stepwise variation of the isohaline level. The procedure is illustrated in Figures 13 and 14. The corresponding velocity signal would either jump or drop, depending on the velocity at the upper layer, since the wave was a depression wave. A schematic showing how a localized initial wave form or bore, $\eta(x, 0)$, evolved into a group of solitons is presented in Figure 14. Following the solitary waves, there was evidence of other nonlinear events (e.g., bores) which originated near station C. Although the available data extended over 2-3 weeks, the solitary waves occurred only during the spring tide period and at the beginning of ebb. As shown in Figure 4, spring tides began on April 21, reached their peak on April 23 and 24, then started to decrease on April 26. The corresponding solitary wave generation occurred during this period, probably because of the weakened stratification due to velocity shear induced mixing. As discussed in section 3, the stronger flow during the spring tide resulted in supercritical flow, which favored the formation of stronger bores and hence solitary waves.

Three sets of solitary wave packets from our observations will be discussed in the next section.

THEORETICAL MODEL FOR INTERNAL SOLITARY WAVES

Interface depth was about 3m at station B. A linear wave phase speed of 0.54 m/s can be estimated using two-layer internal long wave theory. Since the observed wave period is about 3-6 min, the shortest horizontal scale of the wave must be of the order of 97-194 m. Thus, the wave appeared to be long with respect to the total depth. At the same time, we have $h/H<\lambda$ (H=43 m), so that the shallow water approximation, and, hence the KdV equation, is valid in our case.

In terms of the undisturbed density distribution, $\rho(z)$ and the stream function perturbation, *Benny*'s [1966] analysis yielded a KdV type equation of first order in amplitude, similar to

$$A_t + C_0 A_x + \mu A A_x + \delta A_{xxx} = 0 \qquad (14)$$

In equation (14), the subscript denotes differentiation, t is time, x is horizontal position and C_0 is a linear long wave speed. The vertical displacement amplitude is

$$\eta = A\,(x,t)\,\phi\,(z) \qquad (15)$$

where A is the amplitude of the vertical displacement, and $\phi\,(z)$ is

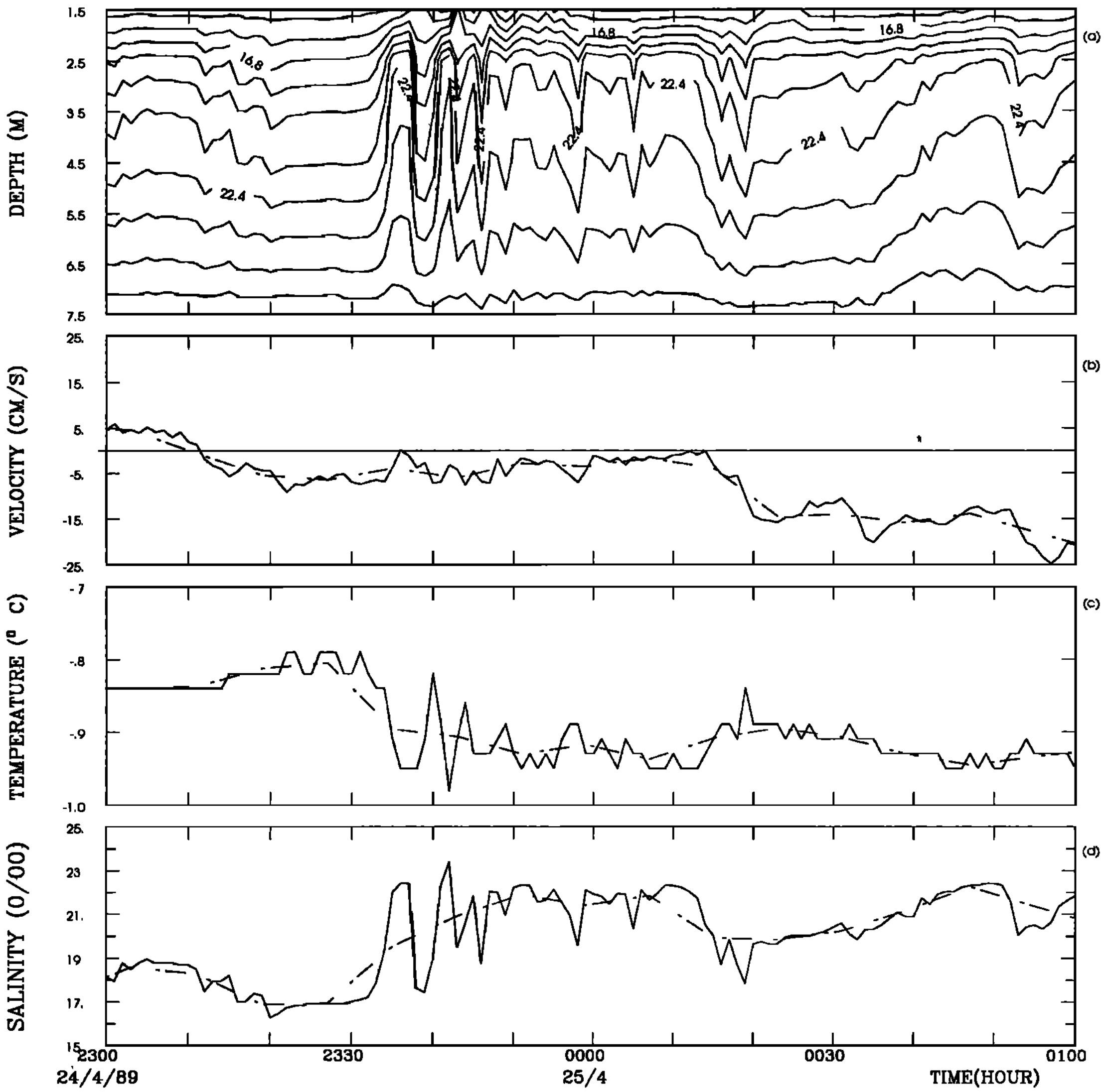

Fig. 13. Expanded time series plots of salinity fluctuations at station B on April 24, 1989. (*a*) Computed isohaline contours based on an interpolation of observations at discrete depths. (*b-d*) Data at 2.5 m for station B. The dashed line is the low pass filtered data set for each series.

the modal function, which will be defined subsequently. The solution to the eigenvalue problem [*Gear and Grimshaw*, 1983] is

$$(\rho_0 (C_0 - U_0)^2 \phi_z)_z + \rho_0 N^2 \phi = 0 \qquad 0<z<H \qquad (16)$$

$$\phi = 0 \qquad z=0 \qquad (17)$$

$$\phi = p\,\sigma (C_0 - U_0)^2 \phi_z \qquad z=H \qquad (18)$$

The fluid is bounded below by the seafloor at $z=0$ and above by a rigid ice cover at $z=h$ (Figure 15). Parameters $\rho_0(z)$ and $U_0(z)$ are density and velocity, respectively. $N^2(z)=(-g/\rho_0)(\partial\rho_0/\partial z)=-(\sigma\rho_0)^{-1}\rho_{0z}$ is the Brunt-Vaisala frequency. Here, σ is small in the Boussinesq approximation. The number p is zero or 1 according to whether the upper boundary is rigid or free, respectively, and is equal to zero in the ice-covered sound. The coordinate system is shown in Figure 15. The linear wave phase speed C_0 is obtained from equation (16), and the coefficients in the KdV are given by

TABLE 3. Observed Solitary Wave Period and Amplitude

Series	Date	Time	Period, min	Amplitude, m
1	April 21	0948-1036	3.2	1.2
2	April 23	1050-1126	5.1	2.1
3	April 24	1118-1224	6.0	1.9
4	April 24	2326-0028	4.0	2.2
5	April 25	1140-1201	4.6	2.2
6	April 26	0002-0038	3.0	1.8
Mean value			4.2	1.9

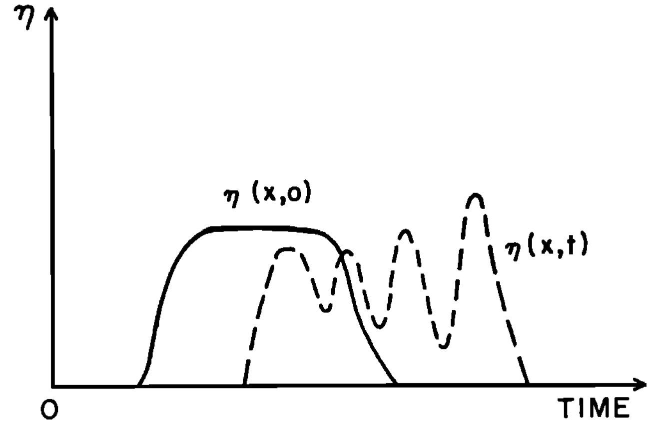

Fig. 14. Schematic showing how an initial bore can evolve into a group of solitary waves. Solid line refers to initial wave form.

$$\mu = \tfrac{3}{2}\left(\int_0^H \rho_0 (C_0 - U_0)^2 \phi_z^3 dz\right) / \left(\int_0^H \rho_0 (C_0 - U_0)\, \phi_z^2 dz\right) \quad (19)$$

$$\delta = \tfrac{1}{2}\left(\int_0^H \rho_0 (C_0 - U_0)^2 \phi^2 dz\right) / \left(\int_0^H \rho_0 (C_0 - U_0)\, \phi_z^2 dz\right) \quad (20)$$

where $C = C_0 + C_1$, $C_1 = (1/3)\mu a$, $L^2 a = 12\delta/\mu$, a is the soliton amplitude, and L the length scale of the wave. The solution for the KdV is $A(x-ct) = a\mathrm{Sech}^2(x-ct)$. Since $U_0(z)$ was very small when solitary waves occurred, it is neglected in our model. The situation with a critical level ($C_0(z) = U_0(z)$) has been discussed by *Liu and Benny* [1981].

We first approximate the density profile, for simplicity, as a two-layer model (Figure 15). The steady state solitary wave solutions, with upper and lower depth h_1 and h_2 and density ρ_1 and ρ_2, are [*Osborne and Burch*, 1980]

$$C_0 = (g' h_1 h_2 / H)^{1/2} \quad (21)$$

$$\mu = 3C_0(h_2 - h_1)/2h_2 h_1 \quad (22)$$

$$\delta = C_0 h_1 h_2 / 6 \quad (23)$$

$$C = C_0 - a\mu/3 \quad (24)$$

$$L = (-12\delta / a\mu)^{1/2} \quad (25)$$

By using the values in Tables 3 and 4, Figure 16 shows the parameter values associated with both first- and second-order KdV for a two-layer fluid [*Gear and Grimshaw*, 1983]. In order to compare the model with observation, wavelength is defined by the point at which the displacement has dropped to 10% of the maximum, or $\lambda = 3.6L$, as *Holloway* [1987] suggested. The observed wave periods were estimated from the salinity oscillations corresponding to the definition of wavelength.

In Figure 16, C/C_0 is about 1.2, so that the nonlinear correction to the linear phase was large. However, the calculated wave periods do not agree well with observations for the first-order model. Based on experimental results in a two-layer fluid, *Koop and Butler* [1981] concluded that the first-order theory was valid for wave amplitudes such as $\varepsilon = a/h_1 \leq 0.2$. The inclusion of second-order nonlinear terms extends the useful range of the two-layer KdV theory to wave amplitudes of $\varepsilon = 0.8$. In our case, the ε were 0.7, 0.7, and 0.6 for the three leading waves, respectively, as shown in Table 4. Therefore, it is necessary to have a second-order term correction in the two-layer KdV model. The results show that the second-order correction is significant, as seen in Figure 16. The correction to phase speed is nearly the same size as the first-order correction but opposite, according to the results of *Sandstrom and Elliott* [1984] *and Holloway* [1987]. Hence the second-order phase speed was approximately the same as the linear phase speed. When the second-order nonlinear term is included, the two-layer model is quite adequate to describe solitary waves in the sound.

To further understand solitary waves and the relationship between the density structure and wave solutions, internal waves at the pycnocline of a continuously stratified fluid were examined. A hyperbolic-tangent density profile is used to approximate the continuously stratified case [*Kao et al.*, 1985]

$$\rho(z) = \rho_0(1 - \varpi \mathrm{Tanh}\alpha\,(z - h_2)) \quad (26)$$

where $\rho_0 = 0.5(\rho_1 + \rho_2)$, $\varpi = (\rho_2 - \rho_1)/2\rho_0$, z is the vertical coordinate (Figure 15), and α^{-1} is a representive half-depth of the pycnocline thickness (Figure 17). Here, ρ_1 and ρ_2 have same value as in the two-layer approximation. By solving equations (16), (17), and (18), we can find the solution for the modal function $\phi(z)$. This eigenvalue problem is solved numerically in a normalized coordinate with $z=0$ at the bottom and $z=43$ m at the top. According to *Kao et al.* [1985], the lowest eigenfunction mode has a maximum phase speed at the interface and corresponds to the interfacial internal wave, while the next mode corresponds to the "bulge-type" wave. It is shown that the higher-order modes have phase speeds much smaller than the speed of the leading wave. In our case, the second-mode speed in group 4 of Table 3 is 0.4 m/s less than that for the first mode and does not satisfy our observations. For comparison, the second-mode eigenfunction on April 24 (group 4) is also presented in Figure 18.

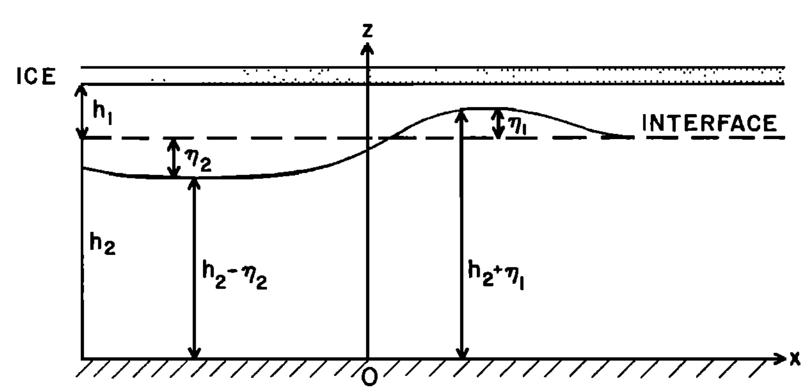

Fig. 15. The coordinate system for KdV.

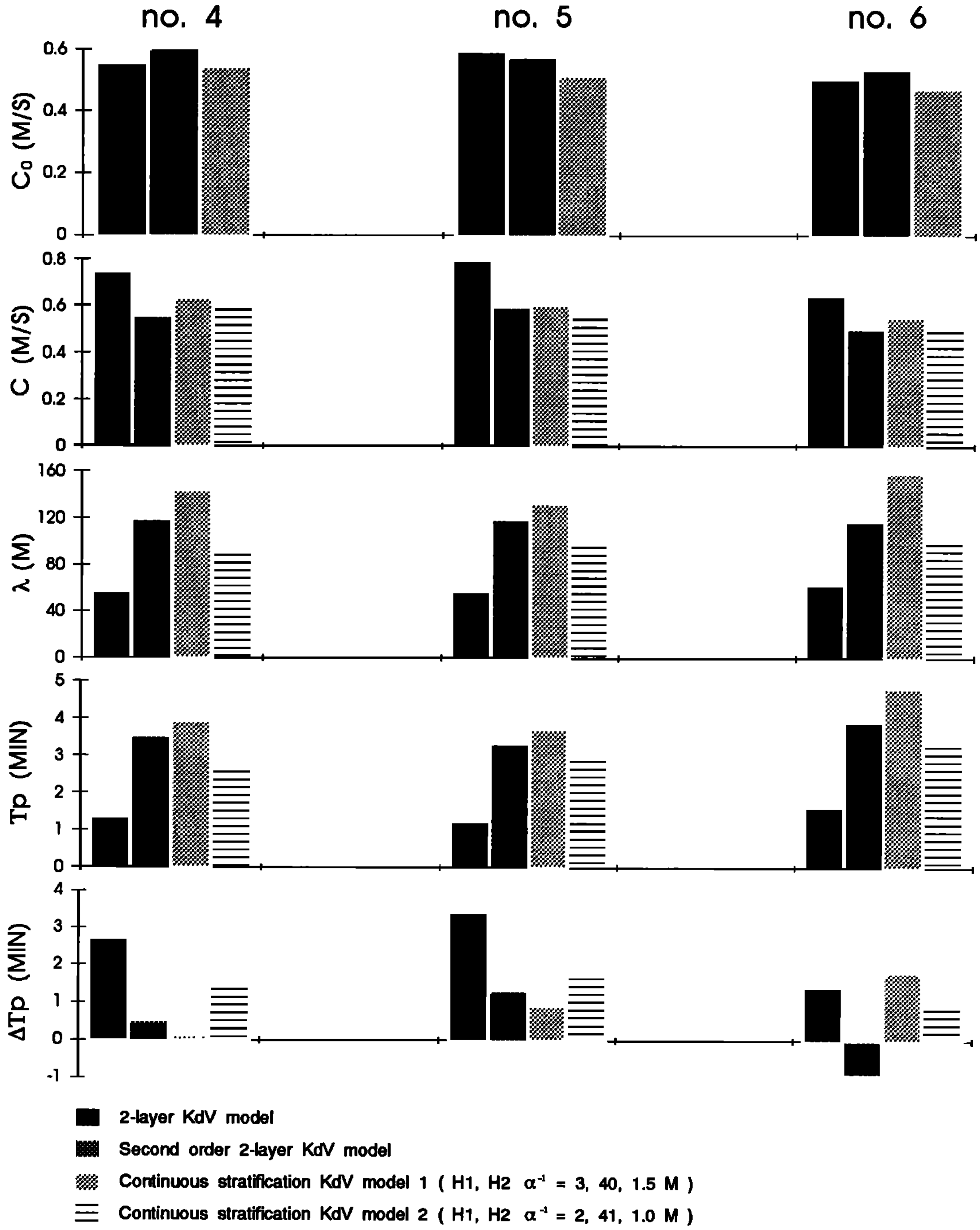

Fig. 16. The linear wave speed C_0, solitary wave speed C, wavelength λ and period T_p for KdV model with different stratification. ΔT_p is the difference between observed and calculated periods.

The eigenfunctions for groups 5 and 6 are similar to group 4. With zero-order eigenfunction $\phi(z)$ and solid surface, but without considering mean flow, the μ and δ in equations (19) and (20), and hence C and L of the solitary wave, can be solved.

Using the values in Tables 3 and 4, Figure 16 also presents the corresponding solitary wave parameter values for two hyperbolic-tangent density profiles. Two different density profiles used in the model for group 4 and the profile on April 29 are plotted in Figure 19. The shape of the density profiles used for groups 5 and 6 was quite similar to that for group 4.

TABLE 4. The Layer Depth, Density, and Parameter $\varepsilon(a/h_1)$ for Three Series

Series	h_1, m	h_2, m	ρ_1, Kg/m^3	ρ_2, Kg/m^3	ε
4	3.0	40.	1010.66	1022.04	0.7
5	3.0	40.	1011.30	1022.36	0.7
6	3.0	40.	1012.76	1022.07	0.6

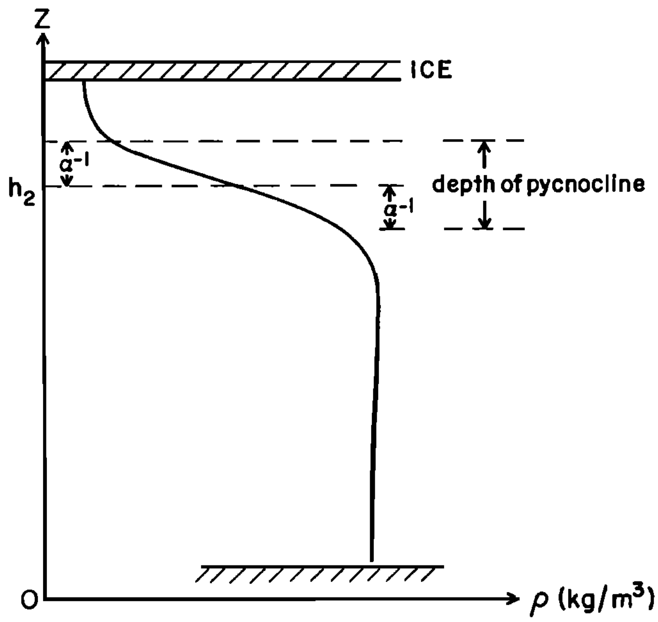

Fig. 17. Typical hyperbolic-tangent density profile.

The results for the continuous stratified case in Figure 16 compare reasonably well with our measurements. The ΔT_p (the difference of observed and calculated periods) in solitons group 4 and 5 is generally small, especially for h_1=3 m, α^{-1}=1.5 m. However, ΔT_p in group 6 is larger when h_1=3 m and α^{-1}=1.5 m than when h_1=2 m and α^{-1}=1.0 m. This implies that the pycnocline might be thinner and shallower (i.e., smaller α^{-1} and h_1) at this time. In fact, soliton group 6 occurred just after the peak spring tide. The tidal range was about 0.5 m smaller than the peak value. The relatively smaller shear and hence weaker mixing might have caused a shallower pycnocline. If neap tide density profiles are applied, C=0.39 m/s, λ=474 m, which are far from our observation. This implies a difference in density profiles between spring and average tides. It should be noted that we did not include the second-order term in the continuously stratified KdV. Thus, wave periods from the first-order continuous stratification KdV may be even closer to the observed values than the second-order KdV equation. *Kao et al.* [1985] also found that quantitative results of the continuously stratified model were substantially different from those of the two-layer model for all important wave parameters. Indeed, the critical value of ε over which the second-order nonlinear term must be considered seems to be larger for the continuous stratification model than for the two-layer case in Kao's results. By comparing several model results in Figure 16, one

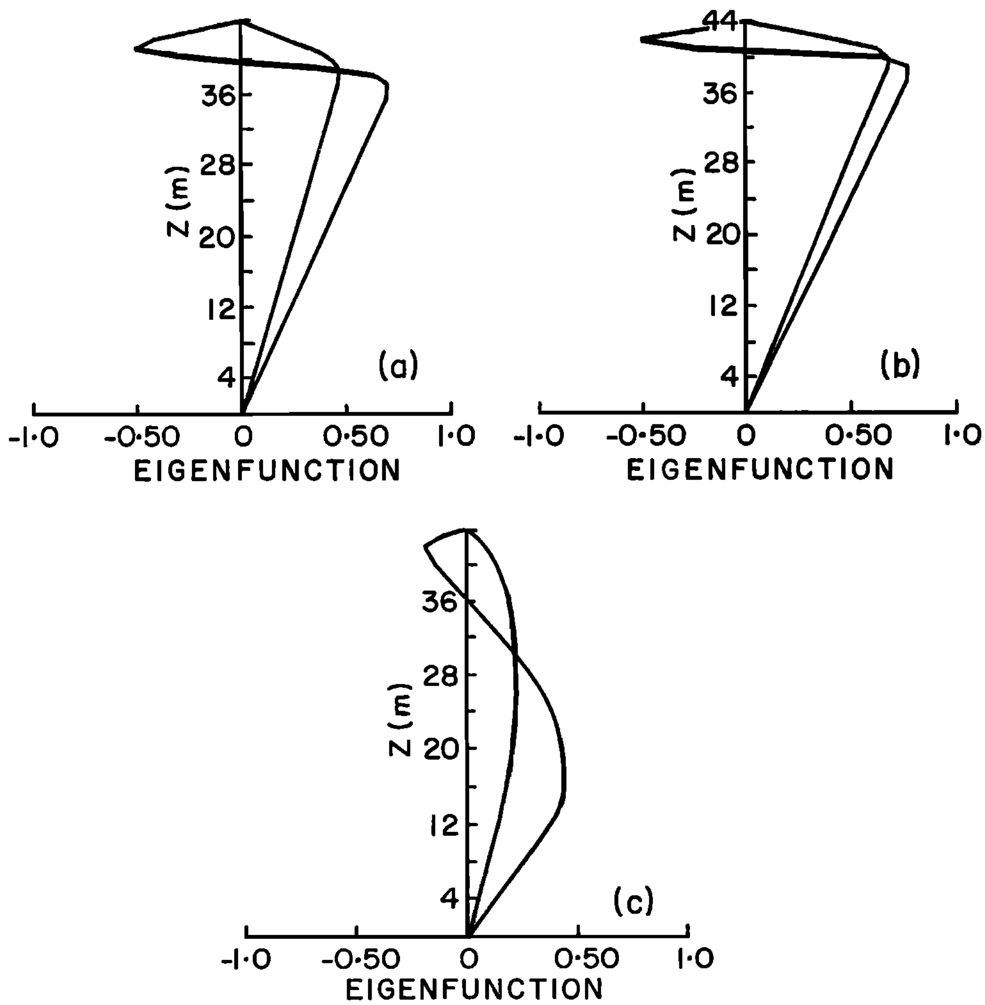

Fig. 18. Shape of eigenfunction $\phi(z)$ for (*a*) h_1=3 m, α^{-1}=1.5 m on April 24, 1989, (*b*) for h_1=2.0 m, α^{-1}=1 m on April 24, 1989, and (*c*) for density profile on April 29.

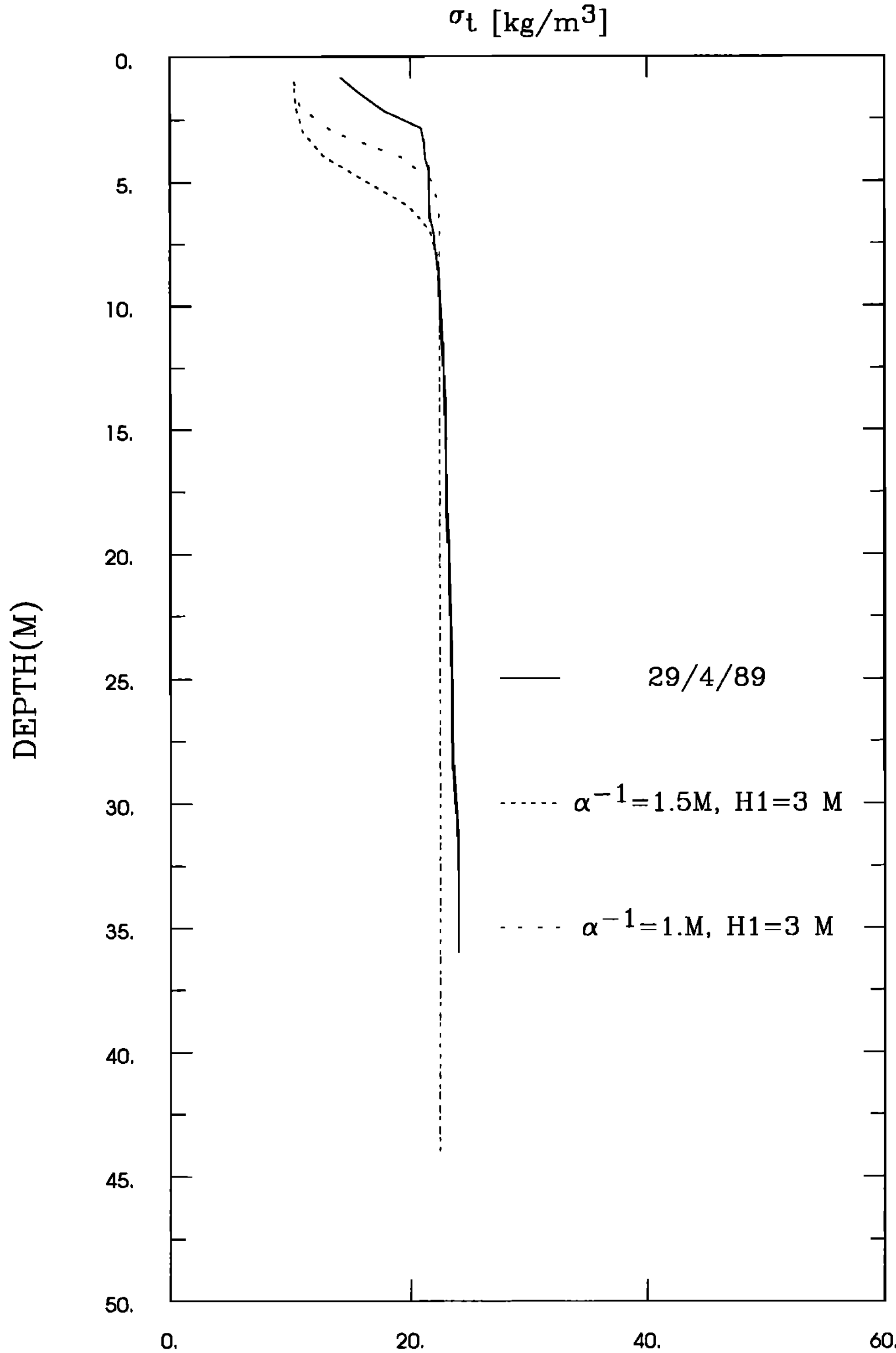

Fig. 19. Three typical density profiles, one from density profile on April 29, 1989, and two from the hyperbolic-tangent density profile with different α^{-1} and h_1, and used for group 4 soliton.

finds that both the continuous density model and the second-order two-layer underpredict the wave period. The continuous density model has a larger phase speed and a longer wavelength than the two-layer model. All agree quite well with observations.

Since the solitary wave phase speed was larger than the general background flow speed, the waves will propagate continuously upstream of station B, as mentioned before. Because the wave speed is proportional to the amplitude (equation (24)), the leading wave with the largest amplitude travels the fastest. The second soliton had the second largest amplitude, and so on. The waves gradually separate from each other when they propagate further upstream because of their different speeds. To address this problem, a time dependent KdV model, with the bore as an initial condition, needs to be used. The propagation speed of the bore from station C to B can be estimated as 0.4 m/s, which is close to the calculated solitary wave speed. In other words, the propagation of a bore is also

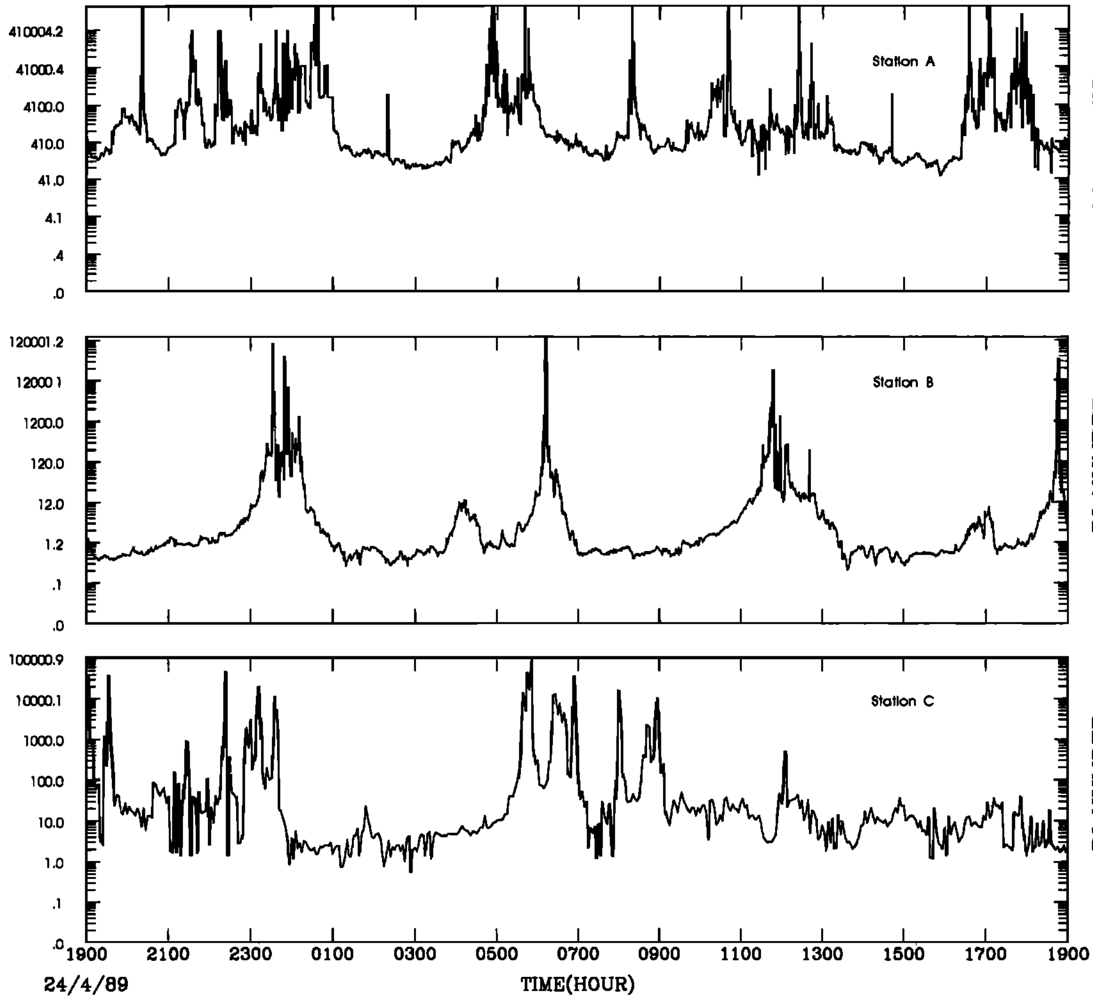

Fig. 20. Time series of Richardson number for stations A, B, and C. The vertical axis is "log" scale.

governed by nonlinear effects. Note, we have already taken into account the effects of background flow.

MIXING IN THE SOUND

As discussed in section 2, salinity generally increased from station A to C at the 1.5 m level and from station B to C at the other observation depths. Horizontal advection of higher salinity water from outside of the sound which could cause these salinity distributions along the sound was assumed negligible. In this section, the following mechanisms, which might contribute to the salinity regime along the sound, will be considered.

1. Strong velocity shear at the narrowest section of the sound could generate a Kelvin-Helmholtz shear instability.

2. Critical and supercritical flow during the flood may result in intense mixing regions which would be advected upstream when the tide turned to ebb.

3. Dissipation of the solitary waves and bores transferred their energy into mixing.

In steady and laminar flow, stability can be measured in terms of the gradient Richardson number, *Ri*, defined by

$$Ri = -\frac{g}{\rho}\frac{\partial\rho/\partial z}{(\partial u/\partial z)^2} \tag{27}$$

where u is the horizontal velocity, z the vertical coordinate upwards, and ρ the density. *Miles* [1961] showed that the condition for stable flow was $Ri > 1/4$ in the presence of small disturbances. When $Ri < 1/4$ at some level in the fluid, the flow is not necessarily unstable. However, many examples of simple shear flow [*Miles*, 1963] did become unstable for some disturbances whenever $Ri < 1/4$. The unstable flow often occurs near the region in which $\partial^2 u/\partial^2 z$ changes sign.

An examination of *Ri* variability at stations A, B and C over a tidal cycle during the spring tide is shown in Figure 20. The *Ri* at station C is averaged in every 3 min to delete high-frequency noise. *Ri* at station A was generally large, and the fluid relatively stable. The smallest *Ri* at stations B and C were reached when the flow at the upper and lower layers had maximal velocity for both stations. The *Ri* here were calculated from related values at 2.5 m and 7.5 m and do not include smaller scale features.

The bores which formed near stations B and C affected the mixing processes in the sound because they deformed the basic flow and might have induced large velocity gradients locally. As a result, the *Ri* and the stability of the flow would be reduced drastically. The *Ri* for the two-layer case can be expressed as

$$Ri = -g'\frac{h_1 + h_2}{(u_2 - u_1)^2} \tag{28}$$

According to the definition of composite Froude number G^2 (equation (3)), the internally subcritical flow is satisfied with the stable condition, or when $G^2 < 1$, $Ri > 1/4$. An instability is possible in the

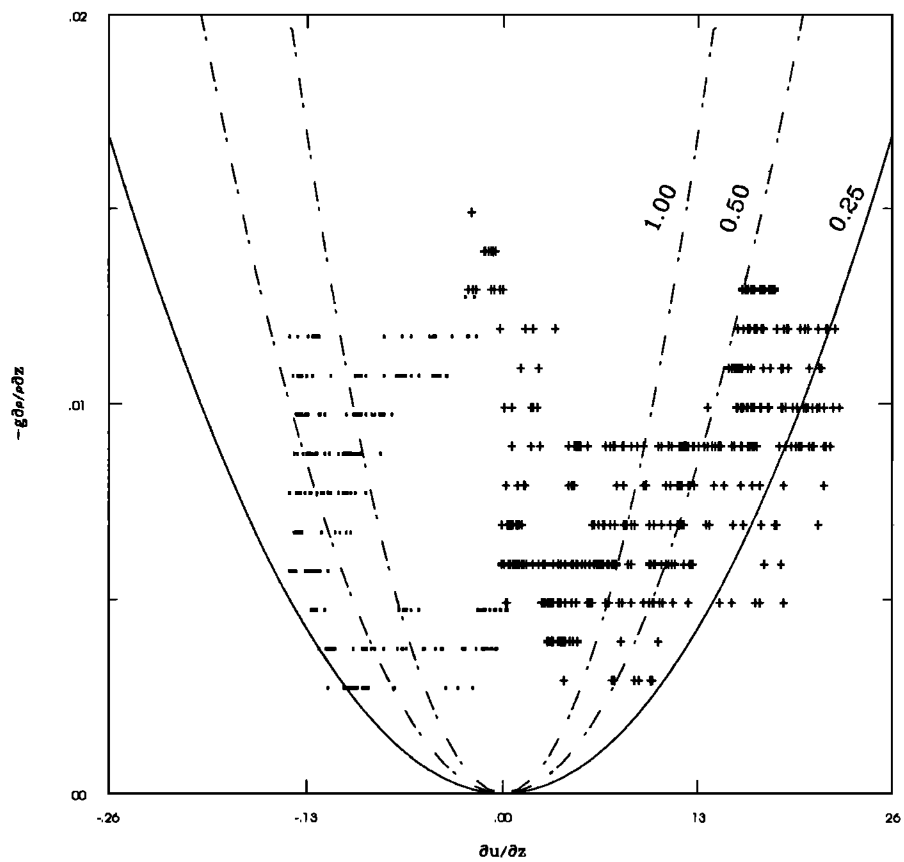

Fig. 21. Richardson number at station B in the velocity shear (∂u/∂z) and density gradient ($g\partial\rho/\rho\partial z$) plane. Pluses refer to Ri during ebb, and negative sign refers to flooding.

region with higher composite Froude number. In our case, the bores were formed near stations B and C when the flow was supercritical. The critical flow at station B occurred simultaneously with the lowest Ri (Figures 11 and 20), although there was only a trough of Ri for supercritical flow at station C. However, the smaller Ri should be upstream of station C, that is, upstream of the bores according to *Lawrence* [1985] and *Rajaratnam and Subramanyan* [1985]. The increased separation of isohalines observed at stations B and C when bores, drops or supercritical flow were present (Figures 9b and 9c) also implies increased vertical mixing at these times. In a quantitative sense, we can calculate the critical velocity shear by using the time-constant hyperbolic-tangent density profile similar to before.

$$\left(\frac{\partial u}{\partial z}\right)_{\text{critical}} = \left(\frac{16g\alpha\varpi}{(1-\varpi\tanh\alpha z)\,(e^{\alpha z}+e^{-\alpha z})}\right)^{1/2} \qquad (29)$$

Substituting the parameters for lowest Ri, the $(\partial u/\partial z)_{\text{critical}}$ is about 0.16 s^{-1} at the mid-pycnocline. If $\partial u/\partial z < (\partial u/\partial z)_{\text{critical}}$, the flow is stable. On the other hand, the density gradient also influences Ri. The relationship between the velocity shear $\partial u/\partial z$ and density gradient $g\partial\rho/\rho\partial z$ is plotted in Figures 21 and 22 for stations B and C, respectively. Figure 21 shows that most of the Richardson numbers ranged over $0.25 < Ri < 0.5$ with smaller Ri during the ebb. Most of the $\partial u/\partial z$ at this Ri range were larger than 0.1 s^{-1}, which agrees well with the critical value calculated from the hyperbolic-tangent density profile. Although the density gradient increased rapidly when $\partial u/\partial z > 0.13$ s^{-1}, the strong shear effect still dominated Ri numbers and kept them below 0.5 during the ebb, during which a bore was observed at station B. Most Ri ranged between 1 and 0.5 during the flood, due to the weaker shear flow. At station C (Figure 22), small Ri occurred during both flood and ebb when the vertical density gradient was small. $\partial u/\partial z$ was smaller compared to station B, and hence Ri was larger.

Figure 8 showed a salinity difference between stations B and A. At the 1.5 m level, salinity increased from station A to B. However, the negative (S_B-S_A) during spring tides at the 2.5 m level suggests that a saltier water source might exist between stations B and A at this level and be advected to station A during the ebb. Comparing data of station A with station B, one finds that solitary-like waves and bores were dissipated between these two stations during each tidal cycle. We expect that part of the dissipated energy both from bores and solitary waves would increase the potential energy of the fluid. Adopting the method used by *Sandstrom and Elliott* [1984], the energy dissipation can be roughly estimated as follows: for a soliton, the total energy is calculated from E_s=(4/3)$g\Delta\rho a^2\lambda$. With a=2.2 m, λ=131 m and $\Delta\rho$=11.1 kg m^{-3} in our case, E_s was 1.3x10^5 J/m of crest length. According to *Osborn* [1980], only 15-20% of energy per unit length would be transferred into an increase of potential energy of the water column. If one assumes that the wave propagation speed was constant and dissipation 1-5 km away from station B, it can be shown that an increase of mixed layer depth of about 0.03-0.3 m resulted during the wave dissipation period according to $\Delta(PE)=1/2g'\rho h_1(\Delta h_1)$. It is obvious that if the dissipation distance was less than 1 km, the increase of mixed layer depth would be larger than 0.3. Since a packet of solitons consisted of three to six single waves, the soliton energy available for increasing the potential energy of the water column would be larger. Similarly, based on *Su*'s [1976] model, the energy loss of an individual bore (the bores which did not decompose into solitons) from

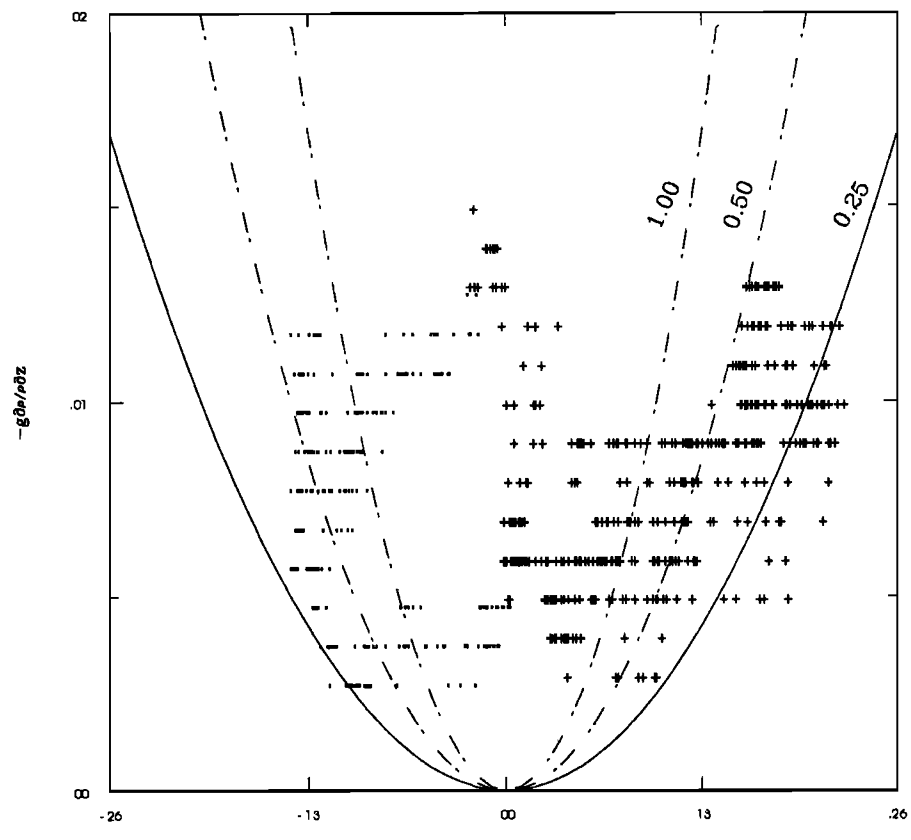

Fig. 22. Richardson number at station C in the velocity shear ($\partial u/\partial z$) and density gradient ($g\partial\rho/\rho\partial z$) plane. Pluses refer to Ri during ebb, and negative sign refers to flooding.

station C during the flood to a region between A and B during the ebb was about 5×10^5 J/m. This seems quite close to the total energy of five solitary waves in the sound. We can therefore argue that the solitary waves and the following bores resulted in increased mixing as they dissipated between stations B and A.

It should be noted that vertical mixing was enhanced in the area where the solitary waves were observed according to the increased separation of isohalines in Figure 9b. This saltier water was advected upstream with the ebb.

CONCLUSIONS

Flow through a horizontal constriction and around sill-like island in the sound is studied based on two-layer hydraulic theory. The observed asymmetry and rapid transition of the interface depth are well explained in terms of the hydraulic characteristics of the flow.

Although both the sill-like island and constriction influenced the hydraulic characteristics along the sound, the constriction (bore generation) had more effect on the upper layer and the sill-like island (drop generation) on the lower layer. Controls on flow exchange varied with tidal phase. Both island and constriction controlled the flow during the tidal stage of case 2, but only one of them controlled the flow for cases 1 and 3. Therefore, tidal forcing is crucial to hydraulic control. However, the whole system, which contained internal bores, drops and solitons along the sound, may be unsteady most of the time and can be regarded as quasi-steady only in certain regions. The steady flow may only occur during the maximum flow (supercritical flow) near the control region [Geyer, 1990]. Although the steady hydraulic theory is used to describe hydraulic controls near the constriction during the maximum flow, the time dependent problem should be introduced to solve the entire problem. As indicated by *Bryden* [1991], "unless this is done, the close agreement of the steady models with many important aspects of the strait will remain a puzzle".

To understand both development of bores (drops) and generation of the solitary waves, it is necessary to link the studies of hydraulics and nonlinear waves. Our analysis shows that solitary waves were generated from the upstream propagating bores. The consequence of hydraulic control is one of the preconditions for soliton generation. Comparisons of several KdV models in terms of different stratification approximations reveal that the KdV model is sensitive to the stratification chosen. The continuous stratification model should be more suitable in explaining the nonlinear wave field. Since density profiles varied dramatically both in time and space, the estimated values of h_1, h_2 (both for two layer and continuous models) and α^{-1} will create a deviation between model results and observation. In fact, the density change will modify the linear wave speed C_0 in equation (16), nonlinear coefficient μ and dispersion coefficient δ in equations (19) and (20). This may, in turn, explain why some bores decomposed into solitary waves and others did not.

The mechanism for mixing along the sound is the combined effect of Kelvin-Helmholtz instability, internal bores and solitary waves. The region of critical and supercritical upper layer flow, the presence and dissipation of the solitary waves and bores were the major causes for the along-channel salinity distribution over a semi-diurnal tidal cycle in the sound.

Acknowledgments. We would like to thank Paul Peltola, Claude Belanger, D. Lachance, and Joshua Sala for their efforts in collecting and processing the original data. Thanks also to D. M. Farmer, T. Warn, and J. Sheng for helpful discussions, and to S. Prinsenberg for comments on the manuscript. Special thanks go to J. C. Croteau, A. Vander Baaren, and Ursula Seidenfuss for data processing and assistance. This work was partially supported by grants from NSERC and Fonds FCAR to R.G.I. and is a contribution to the program of the Group Interuniversitaire de Recherche Océanographique du Québec. The Department of Fisheries and Oceans (Canada) provided logistical support.

REFERENCES

Armi, L., The hydraulics of two flowing layers with different densities, *J. Fluid Mech.*, *163*, 27-58, 1986.

Armi, L., and D.M. Farmer, The internal hydraulics of the Strait of Gibraltar and associated sills and narrows, *Oceanologica Acta*, *8*, 37-46,1985.

Armi, L., and D.M. Farmer, Maximal two-layer exchange through a contraction with barotropic flow, *J. Fluid Mech.* , *164*, 27-51, 1986.

Armi, L., and D.M. Farmer, Generation of the concept of maximal exchange in a strait, *J. Geophys. Res.*, *92* (C13), 14,679-14,680, 1987.

Armi, L., and D.M. Farmer, The flow of Mediterranean water through the strait of Gibraltar, *Prog. Oceanogr.*, *21*(1), 1988.

Baines, P.G., A unified description of two-layer flow over topography. *J.Fluid Mech.*, *146*, 127-167, 1984.

Benjamin, T.B., Internal waves of finite amplitude and permanent form. *J.Fluid Mech.*, *25*, 241, 1966.

Benny, D.J., Long non-linear waves in fluid flows, *J. Math. Phys.*, *45*, 52-63, 1966.

Bryden, H.L., Recent progress in strait dynamics, *Rev. of Geophys.* suppl., 617-631., 1991.

Farmer, D.M., Observation of long nonlinear internal waves in a lake, *J. Phys. Oceanogr.*, *8*(11), 63-73, 1978.

Farmer, D.M., and L. Armi, Maximal two-layer exchange over a sill and through the combination of sill and contraction with barotropic flow, *J. Fluid Mech.*, *164*, 53-76, 1986.

Farmer, D.M., and L. Armi, The flow of Atlantic water through the Strait of Gibraltar, *Prog. Oceanogr.*, *21*(1), 1988.

Farmer, D.M., and R.A. Denton, Hydraulic control of flow over the sill in Observatory Inlet, *J. Geophys. Res.*, *90*, 9051-9068, 1985.

Farmer, D.M., and J.D. Smith, Non-linear internal waves in a fjord, in *Hydrodynamics of Estuaries and Fjords*, edited by J.C.J. Nihoul, pp. 465-493, Elsevier, New York, 1978.

Gan, J.P., Internal hydraulics, solitons and associated mixing in a stratified sound, M.Sc. thesis, 73 pp, McGill University, Montreal, Canada, 1991.

Gardner, G.B., and J.D. Smith, Turbulence mixing in a salt wedge estuary, in *Hydrodynamics of Estuaries and Fjords*, edited by J.C. J. Nihoul, pp. 79-106, Elsevier, New York, 1978.

Gear, J.A., and R.H.J. Grimshaw, Second-order theory for solitary waves in shallow fluid, *Phys. Fluids*, *26*, 14-29, 1983.

Geyer, W.R., Time-dependent, two-layer flow over a sill, in The *Physical Oceanography of Sea Straits*, edited by L.J. Pratt, 421-432, Kluwer, Boston, 1990.

Grimshaw, R.H.J., Long nonlinear internal waves in channels of arbitrary cross-section, *J. Fluid Mech. 86*, 415-431, 1978.

Halpern D., Observation on short-period internal waves in Massachusetts Bay, *J. Mar. Res.*, *29*, 116-132, 1969.

Haury, L., G. Briscoe, and M. Orr, Tidally generated internal wave packets in Massachusetts Bay, *Nature*, *278*, 312-317, 1979.

Holloway, P., Internal hydraulic jumps and solitons at a shelf break region on the Australian northwest shelf, *J. Geophys. Res.*, *92*, 5405-5416, 1987.

Hogg, N.G., Multilayer hydraulic control with application to the Alboran Sea circulation, *J. Phys. Oceanogr.*, *15*, 454-466, 1985.

Ingram, R.G., Characteristics of the Great Whale River plume, J. Geophys. Res., *86*(c3), 2017-2023, 1981.

Ingram, R.G., Salt entrainment and mixing processes in an under-ice river plume, *Coastal Oceanography*, edited by H. G. Gade, A. Edwards, and H. Svendsen, 586 pp, Plenum, New York, 1983.

Ingram, R.G., J.C. Osler, and L. Legendre, Influence of internal wave induced vertical mixing on ice algal production in a highly stratified sound, *Estuarine Coastal Shelf Sci.*, *29*, 435-446,1989.

Ivanov, V.A., and K.V. Konyaev, Bore on a thermocline, *Izv.Akad. Nauk SSSR Fiz. Atmos. Okeana*, *12*(4), 416-423, 1976.(*Izv.Acad. Sci. USSR Atmos. Oceanic Phys.*, Engl. Transl., *12*(4), 1976.)

Johnson, R., Some numerical solutions of a variable-coefficient KdV equation, *J. Fluid. Mech.*, *54*, 81-91, 1972.

Johnson, R., On the development of a solitary wave moving over an uneven bottom, *Proc. Cambridge Philos. Soc.*, *73*, 183-203, 1973a.

Johnson, R., On an asymptotic of KdV equation with slowly varying coefficients, *J. Fluid Mech.*, *60*, 813-824, 1973b.

Kao, T.W., F.S. Pan, and D. Renouard, Internal solitons on the pycnocline: Generation, propagation, and shoaling and breaking over a slope, *J. Fluid Mech.*, *159*, 19-53, 1985.

Koop, C., and G. Butler, An investigation of internal solitary waves in a two-fluid system, *J. Fluid. Mech.*, *112*, 225-251, 1981.

Kubota, T., D. Ko, and D. Dobbs, Propagation of weakly non-linear internal wave in a stratified fluid of finite depth, *AIAA. J. Hydronaut.*, *12*, 157-165, 1978.

Larouche, P., Mesures oceanographiques dans le panache de la Grande rivière de la Baleine, hiver 1983, *Rapport statistique Canadien sur l'hydrographie et les science océaniques No. 20*, 706 pp., Fisheries and Oceans, Canada, Quebec, Canada, 1984.

Lawrence, G.A., The hydraulics and mixing of two-layer flow over an obstacle, *Report UCB/HEL-85/02*, University of California, Berkeley, 1985.

Lee, C., and R.C. Beardsley, The generation of long nonlinear internal waves in a weakly stratified shear flow, *J. Geophys. Res.*, *79*, 453-462, 1964.

Lewis, R.E., Intense mixing periods in an estuary, *Turbulence and Diffusion in Stable Environments*, edited by J.C.R. Hunt, 319 pp, Oxford, New York, 1985.

Liu, A., and D. Benney, The evolution of nonlinear wave trains in stratified shear flows, *Stud. Appl. Math.*, *64*, 247-269, 1981.

Long, R.R., Some aspects of the flow of stratified fluids, I, A theoretical investigation, *Tellus* , *5*, 42-57, 1953.

Long, R.R., Some aspects of the flow of stratified fluid, II, Experiments with a two-fluid system, *Tellus*, *6*, 97-115, 1954.

Long, R.R., Some aspects of the flow of stratified fluid, III, Continuous density gradients, *Tellus*, *7*, 342-357, 1955.

Long, R.R., Some experimental observations of upstream disturbances in a two-fluid system, *Tellus*, *26*, 313-317, 1974.

Maslowe, S.A., and L.G. Redekopp, Long non-linear waves in stratified shear flows, *J. Fluid Mech.*, *101*, 321-348, 1980.

Maxworthy, T.A., Note on the internal solitary waves produced by tidal flow over a three-dimensional ridge, *J. Geophys. Res.*, *84*, 338-346, 1979.

Miles, J.W., On the stability of heterogeneous shear flows, *J. Fluid Mech.*, *10*, 496-508, 1961.

Miles, J.W., On the stability of heterogeneous shear flows, 2, *J. Fluid Mech. 16*, 209-227, 1963.

New, A.L., K.R. Dyer, and R.E. Lewis, Internal waves and intense mixing periods in a partially stratified estuary, *Estuarine Coastal Shelf Sci.*, *24*, 15-33, 1987.

Ono, H., Algebraic solitary waves in stratified fluids, *J.Phys. Soc. Jpn.*, *39*, 1082-1091, 1975.

Osborne, A., Estimates of the local rate of vertical diffusion from dissipation measurements, *J. Phys. Oceanogr.*, *10*, 83-89, 1980.

Osborne, A., and T. Burch, Internal solitons in the Andaman Sea, *Science*, *208*, 451-460, 1980.

Partch, E.N., and J.D. Smith, Time dependent mixing in a salt wedge estuary, *Estuarine Coastal Shelf Sci.*, *6*, 3-19, 1978.

Pierini, S., A model for the Alboran Sea internal solitary waves, *J. Phys. Oceanogr.*, *19*, 755-772, 1989.

Rajaratnam, W., and S. Subramanyan, Plane turbulent buoyant surface jets and jumps, *J. Hydraul. Res.*, *23*, 131-146, 1985.

Sandstrom, H., and J. Elliott, Internal tide and solitons on the Scotian Shelf: A nutrient pump at work, *J. Geophys. Res.*, *89*, 6415-6426, 1984.

Sandstrom, H., J. Elliott, and N. Cochrance, Observing groups of solitary internal waves and turbulence with batfish and echo-sounder, *J. Phys. Oceanogr.*, *19*, 987- 997, 1989.

Segur, H., and J. Hammack, Soliton models of long internal waves, *J. Fluid Mech.*, *118*, 285-304, 1982.

Su, C.H., Hydraulic jump in an incompressible stratified fluid, *J. Fluid Mech.*, *73*, 3-47, 1976.

Tung, K., D. Ko, and J. Chang, Weakly nonlinear internal waves in shear, *Stud. Appl. Math.*, 65, 189-221, 1981.

J. Gan and R.G. Ingram, Department of Atmospheric and Oceanic Sciences, McGill University, 805 Sherbrooke Street West, Montréal, Québec H3A 2K6, Canada.

(Received August 9, 1991;
revised February 26, 1992;
accepted February 26, 1992.)